Characterizing the Multiple Protostellar System VLA 1623-2417 with JWST, ALMA, and VLA: Outflow Origins, Dust Growth, and an Unsettled Disk

Isaac C. Radley[1] , Gemma Busquet[2,3,4] , John D. Ilee[1] , Hauyu Baobab Liu[5,6] , Jaime E. Pineda[7] ,
Klaus M. Pontoppidan[8] , Enrique Macías[9] , María José Maureira[10] , Eleonora Bianchi[11] , Tyler L. Bourke[12] ,
Claudio Codella[11] , Jan Forbrich[13] , Josep M. Girart[4,14] , Melvin G. Hoare[1] , Ricardo Hernández Garnica[15] ,
Izaskun Jiménez-Serra[16] , Laurent Loinard[15,17,18] , Jazmín Ordóñez-Toro[15] , and Linda Podio[11]

[1] School of Physics and Astronomy University of Leeds, LS2 9JT, Leeds, UK
[2] Departament de Física Quàntica i Astrofísica (FQA), Universitat de Barcelona, Martí i Franquès 1, E-08028 Barcelona, Catalonia, Spain
[3] Institut de Ciències del Cosmos (ICCUB), Universitat de Barcelona, Martí i Franquès 1, E-08028 Barcelona, Catalonia, Spain
[4] Institut d'Estudis Espacials de Catalunya (IEEC), Esteve Terradas 1, edifici RDIT, Parc Mediterrani de la Tecnologia (PMT) Campus del Baix Llobregat—UPC 08860 Castelldefels (Barcelona), Catalonia, Spain
[5] Department of Physics, National Sun Yat-Sen University, No. 70, Lien-Hai Road, Kaohsiung City 80424, Taiwan, R.O.C.
[6] Center of Astronomy and Gravitation, National Taiwan Normal University, Taipei 116, Taiwan
[7] Max-Planck-Institut für extraterrestrische Physik, Giessenbachstrasse 1, D-85748 Garching, Germany
[8] Jet Propulsion Laboratory, California Institute of Technology, 4800 Oak Grove Drive, Pasadena, CA 91109, USA
[9] European Southern Observatory, Karl-Schwarzschild-Str. 2, 85748, Garching bei München, Germany
[10] Max-Planck-Institut für Extraterrestrische Physik (MPE), D-85748 Garching, Germany
[11] INAF, Osservatorio Astrofisico di Arcetri, Largo E. Fermi 5, 50125 Firenze, Italy
[12] SKA Observatory, Jodrell Bank, Lower Withington, Macclesfield, SK11 9FT, UK
[13] University of Hertfordshire, Centre for Astrophysics Research, College Lane, Hatfield, AL10 9AB, UK
[14] Institut de Ciències de l'Espai (ICE-CSIC), Campus UAB, Carrer de Can Magrans S/N, E-08193 Cerdanyola del Vallès, Catalonia, Spain
[15] Instituto de Radioastronomía y Astrofísica, Universidad Nacional Autonóma de México, Apartado Postal 3-72, Morelia 58090, Michoacán, Mexico
[16] Center of Astrobiology (CAB), CSIC-INTA, Ctra. de Ajalvir km 4, E-28850, Torrejón de Ardoz, Madrid, Spain
[17] Black Hole Initiative at Harvard University, 20 Garden Street, Cambridge, MA 02138, USA
[18] David Rockefeller Center for Latin American Studies, Harvard University, 1730 Cambridge Street, Cambridge, MA 02138, USA

Abstract

Utilizing the James Webb Space Telescope (JWST), the Atacama Large Millimeter/submillimeter Array (ALMA), and the Very Large Array (VLA), we present high angular resolution ($0''06$–$0''42$), multiwavelength (4 μm–3 cm) observations of the VLA 1623-2417 protostellar system to characterize the origin, morphology and, properties of the continuum emission. JWST observations at 4.4 μm reveal outflow cavities for VLA 1623 A and, for the first time, VLA 1623 B, as well as scattered light from the upper layers of the VLA 1623 W disk. We model the millimeter-centimeter spectral energy distributions to quantify the relative contributions of dust and ionized gas emission, calculate dust masses, and use spectral index maps to determine where optical depth hinders this analysis. In general, all objects appear to be optically thick down to $\sim$90 GHz, show evidence for significant amounts (tens to hundreds of $M_\oplus$) of large ($>$1 mm) dust grains, and are dominated by ionized gas emission for frequencies $\lesssim$15 GHz. In addition, we find evidence of unsettled millimeter dust in the inclined disk of VLA 1623 B possibly attributed to instabilities within the circumstellar disk, adding to the growing catalog of unsettled Class 0/I disks. Our results represent some of the highest-resolution observations possible with current instrumentation, particularly in the case of the VLA. However, our interpretation is still limited at low frequencies ($\lesssim$22 GHz) and thus motivates the need for next-generation interferometers operating at centimeter wavelengths.

Unified Astronomy Thesaurus concepts: Star formation (1569); Protoplanetary disks (1300); Young stellar objects (1834)

1. Introduction

The primary mode of planet formation occurs via the successive coagulation and subsequent growth of small ($\sim$0.1 μm) interstellar medium (ISM)-like dust particles through 12 orders of magnitude to planetary scales (e.g., S. J. Weidenschilling 1977). Traditionally, this was thought to be a slow process, and therefore confined to the later stages of evolution in protoplanetary disks, in particular the Class II phase (with ages $\sim$10$^{5.5}$–10^7 yr; I. Pascucci et al. 2023). However, recent theoretical advances have shown that the planet formation process can proceed much more quickly than

originally anticipated, for example, by processes such as the streaming instability (see A. Johansen et al. 2014, for a review). This, coupled with recent observational evidence of possible planet-induced substructure in young disks (e.g., D. M. Segura-Cox et al. 2020), has led to a renewed interest in studying planet formation in the earliest stages of star formation, for example, with recent surveys such as FAUST (Fifty AU STudy of the chemistry in the disk/envelope system of solar-like protostars; C. Codella et al. 2021), eDISK (Early Planet Formation in Embedded Disks; N. Ohashi et al. 2023), and CAMPOS (ALMA Legacy survey of Class 0/I disks in Corona australis, Aquila, chaMaeleon, oPhiuchus north, Ophiuchus, and Serpens; C.-H. Hsieh et al. 2024).

As a result of the dust growth processes previously mentioned, we expect to find a distribution of dust grain sizes in protoplanetary disks. Since thermal emission arises at

wavelengths related to the dust grain size, i.e., $a_{max} \sim \frac{\lambda}{2\pi}$, this means we must utilize observational wavelengths across a similarly broad range in order to fully characterize the dust population in disks. Scattered light has been used to trace approximately micron-sized dust grains, which are coupled to the gas and suspended in the atmospheres of disks (e.g., M. Villenave et al. 2019; C. Ginski et al. 2024) providing constraints on their vertical extent. Longer wavelength observations in the (sub)millimeter regime can begin to trace larger dust that becomes decoupled from the gas, settling toward the planet-forming midplane of the disk (e.g., M. Ansdell et al. 2016; S. M. Andrews et al. 2018). Until recently, it was assumed such observations gave an unobstructed view of the raw material available for planet formation. However, even at these longer wavelengths, significant optical depths can still be reached in the disks due to the high density of material (Z. Zhu et al. 2019; C.-Y. Chung et al. 2024). Moving toward the longest wavelengths in the centimeter regime provides the best chance at mitigating any effects of high optical depth (see, e.g., C. Carrasco-González et al. 2019). Unfortunately, this is complicated by the fact that these observations do not only trace thermal dust emission, but are also sensitive to emission from ionized gas through winds, jets, and magnetospheric processes operating in young stellar objects (YSOs) and their circumstellar disks (see, e.g., H. B. Liu et al. 2014; A. Coutens et al. 2019).

This contribution of ionized gas emission can have significant effects on the derived spectral energy distribution (SED) at low frequencies (e.g., $\lesssim 30$ GHz; S. A. Dzib et al. 2013) with a shape that is unique to the properties driving the emission. We can consider two general regimes for which the ionized gas mechanism is primarily contributing based on the derived SED and therefore spectral index, α, where $F_\nu \propto \nu^\alpha$. In the first case, emission arises from free–free interactions in an ionized gas, which can be located close to the central star such as at the base of a jet, or as a photoevaporative disk wind. In this regime, we expect α values between -0.1 and $+1$ (I. Pascucci et al. 2012; E. Macías et al. 2016; G. Anglada et al. 2018) with a typical value of ~ 0.6 for an idealized jet (see, e.g., S. P. Reynolds 1986). Alternatively, we may also have significant contributions from magnetospheric activity such as gyrosynchrotron emission (E. D. Feigelson & T. Montmerle 1985) where free electrons interact with magnetic field lines originating from the central star giving rise to a nonthermal emission process with a typical $\alpha \sim -0.7$ for stars within the ISM (J. J. Condon & S. M. Ransom 2016). It is important to note that within star-forming regions, the higher-density environment can lead to variations in the observed spectral index value with previous surveys finding $\alpha < -0.1$ for possible nonthermal emitters (e.g., S. A. Dzib et al. 2013) and theoretical predictions demonstrating values potentially as low as -2 (e.g., G. A. Dulk 1985). While these values in theory offer a potential discriminant between emission mechanism, the actual observed α will vary due to its dependence on optical depth and local environment. Therefore, we must obtain high spatial resolution and high-sensitivity observations of YSOs across multiple characteristic wavelengths in order to be able to properly decompose the relative contributions of each of these processes to the observed emission.

The VLA 1623-2417 system (hereafter VLA 1623) is located in the Ophiuchus A (L1688) star-forming region. Ophiuchus is one of the closest star-forming regions at 138.4 pc

(G. N. Ortiz-León et al. 2018) making it an excellent observational candidate for both maximizing spatial resolution as well as sensitivity to ensure faint multiwavelength emission can be detected above the noise level. Due to these favorable characteristics, both the individual YSOs and properties of the region as a whole have been extensively studied (e.g., N. A. Ridge et al. 2006; S. A. Dzib et al. 2013; R. K. Friesen et al. 2017; L. A. Cieza et al. 2019).

The VLA 1623 system is now known to be comprised of four objects—Aa, Ab, B, and West (W).[19] The protobinary system, VLA 1623 A (Aa + Ab), is considered to be the prototypical Class 0 object (P. Andre et al. 1993) and has been found to be surrounded by a circumbinary disk (see, e.g., N. M. Murillo et al. 2013; C.-H. Hsieh et al. 2020; S. I. Sadavoy et al. 2024). Previous observations (see, e.g., N. M. Murillo & S.-P. Lai 2013) classified VLA 1623 A as a single object due to their limited angular resolution until R. J. Harris et al. (2018) and R. Kawabe et al. (2018) were able to successfully resolve the object into two protostellar components separated by $0\overset{''}{.}21$ (~ 30 au; R. J. Harris et al. 2018). In contrast, the nature of VLA 1623 B and VLA 1623 W has previously been subject to debate. Both objects were thought to possibly be shocked cloudlets (S. Bontemps & P. Andre 1997) instead of YSOs. However, recent observations from (sub)millimeter dust continuum (R. J. Harris et al. 2018; A. Michel et al. 2022) and kinematic gas tracers (S. Ohashi et al. 2022; S. Mercimek et al. 2023; C. Codella et al. 2024) point toward embedded, disk-bearing protostars. VLA 1623 B has been suggested to be a Class 0 YSO (N. M. Murillo et al. 2018a) observed to have an inclined protostellar disk ($i > 70°$; S. I. Sadavoy et al. 2019, 2024) and is separated by $\sim 1\overset{''}{.}2$ (~ 170 au) from its companion VLA 1623 A (R. J. Harris et al. 2018). VLA 1623 W is found at a much larger separation to A ($\sim 11'' \sim 1500$ au; S. Mercimek et al. 2023) and is thought to be a slightly more evolved Class I YSO with a nearly edge-on protostellar disk ($i \sim 75°$–$80°$; S. I. Sadavoy et al. 2019; A. Michel et al. 2022; S. I. Sadavoy et al. 2024).

Previous studies of the VLA 1623 system found a large-scale, bipolar outflow in CO and H_2 originating from VLA 1623 A (see, e.g., P. Andre et al. 1990; C. J. Davis & J. Eisloeffel 1995; W. R. F. Dent et al. 1995; A. Caratti o Garatti et al. 2006). More recently, the VLA 1623 A outflow has also been detected in multiple molecular tracers and forbidden lines, e.g., c-C_3H_2 (N. M. Murillo et al. 2018b) and [O I] (B. Nisini et al. 2015). Spitzer (G. G. Fazio et al. 2004) observations at 4 μm revealed a cavity aligned with the outflow in the proximity of VLA 1623 A (see, e.g., M. Zhang & H. Wang 2009; R. Kawabe et al. 2018). Interestingly, VLA 1623 B is theorized to have jet driving a collimated outflow (see, e.g., G. Santangelo et al. 2015); however, no outflow cavity has been detected close to the protostar. Due to their deeply embedded nature (see, e.g., L. W. Looney et al. 2000; N. M. Murillo & S.-P. Lai 2013), neither VLA 1623 A nor B protostars are directly detected in these Spitzer images. Conversely, VLA 1623 W appears as a pointlike infrared source that can been clearly seen in the R. Kawabe et al. (2018) 4.5 μm image as well as at 8 μm and 24 μm in N. M. Murillo & S.-P. Lai (2013).

Unfortunately, due to the proximity of VLA 1623 A and B, the origin of detected outflows has been difficult to attribute to one or multiple objects. Observations of CO(3–2) from

---

[19] Aa and Ab have also been referred to as A1 and A2, respectively; see, e.g., S. Ohashi et al. (2022).
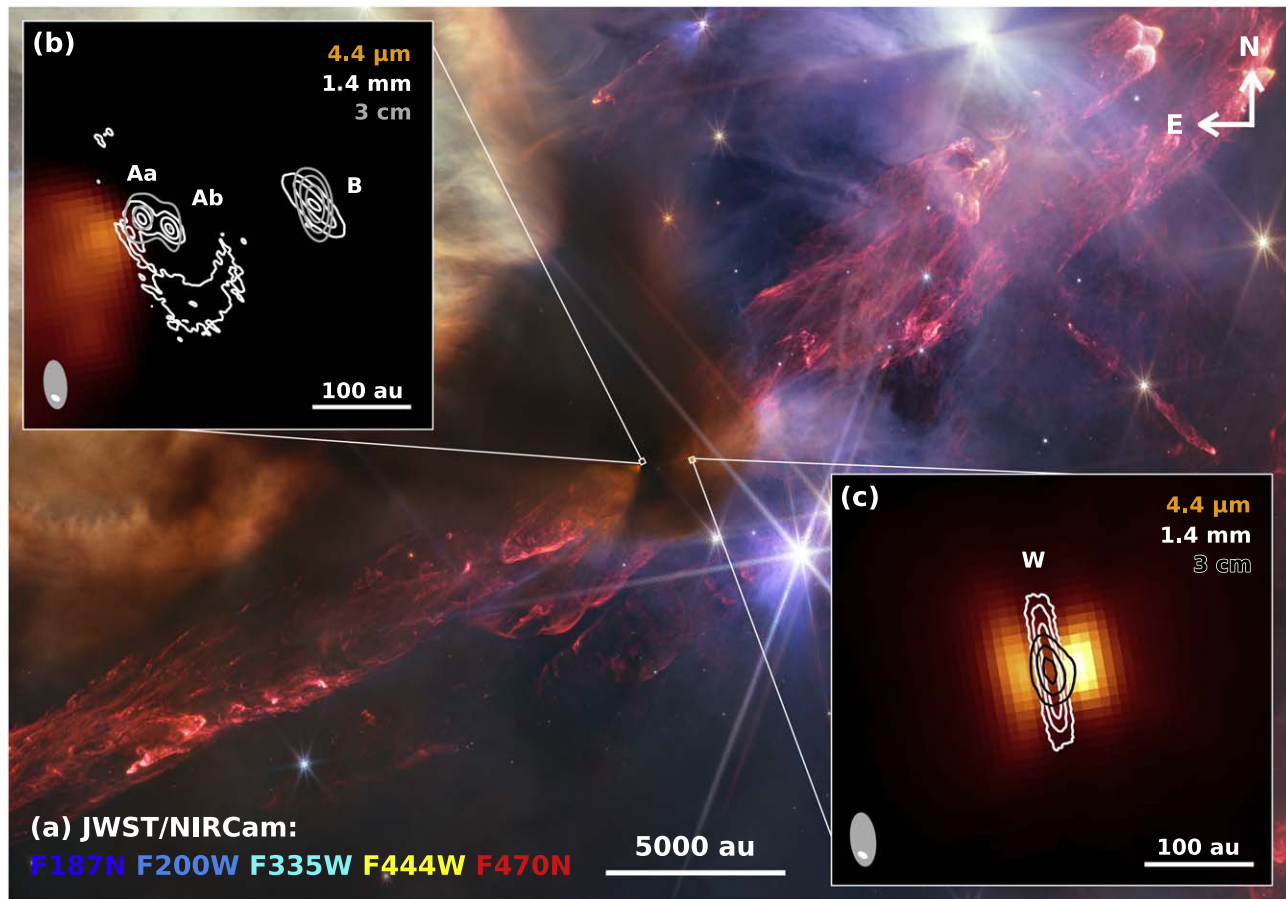
Figure 1. (a) JWST/NIRCam First Anniversary image centered on the VLA 1623 system, showing the parsec-scale bipolar outflows (NASA/ESA/CSA/STScI). (b) Zoom-in toward VLA 1623 Aa, Ab and B. The color scale shows emission from the JWST/NIRCam 4.4 μm filter (peak normalized with a square root stretch) tracing the base of the SE outflow. White contours show the ALMA 1.4 mm (217 GHz) emission dominated by thermal dust emission (8σ, 125σ, 350σ, where $\sigma = 0.02$ mJy beam^{-1}). Gray contours show the VLA 3 cm (10 GHz) emission (7σ, 12σ, 20σ, where $\sigma = 0.01$ mJy beam^{-1}) tracing a combination of thermal dust and ionized gas emission. (c) Zoom-in toward VLA 1623 W. The color scale is as in panel (a), tracing scattered light from the upper layers of the edge-on disk. White contours show 1.4 mm emission (8σ, 25σ, 45σ) and black show 3.0 cm emission (3σ, 5σ, 7σ), which similarly trace thermal dust and a combination of thermal dust and ionized gas, respectively.

C.-H. Hsieh et al. (2020) point toward two outflows being driven by A and B individually whereas observations of ^{12}CO(2–1) in C. Hara et al. (2021) indicate that both outflows may originate from the Aa and Ab in the VLA 1623 A protobinary. Therefore, there is a degree of ambiguity on which specific objects are driving the outflows detected in the VLA 1623 system.

In this paper, we present high-resolution Very Large Array (VLA), Atacama Large Millimeter/submillimeter Array (ALMA), and James Webb Space Telescope (JWST) continuum observations of the VLA 1623 system. We describe our observational setup and final imaging parameters in Section 2. In Section 3 we present our continuum images, fluxes, and derived spectral indices for each object. Additionally, through SED analysis, we probe possible interpretations of the dust and ionized gas populations. We discuss our findings in Section 4, and finally Section 5 gives an overview of our conclusions as well as contextualizing this work in regards to an upcoming wider survey of Ophiuchus expanding on the work of A. Coutens et al. (2019).

2. Observations and Data Reduction

Figure 1 shows an overview of the L1688 region observed with JWST, overlaid with our VLA and ALMA observations of

the VLA 1623 system, demonstrating the connection of these YSOs to the wider star-forming environment. Below, we discuss the observational setup and data reduction steps taken for each of the instruments.

2.1. JWST/NIRCam

A section of the Ophiuchus star-forming region was observed by the near-infrared camera (NIRCam) instrument (M. J. Rieke et al. 2023) on 2023 March 7, April 5, and April 6 to produce the first anniversary image for JWST (PID: 2739, P. I. Pontoppidan). The field covers ~49 square arcminutes and includes the VLA 1623 outflow, as well as several well-studied young stars and protostars. Six filters were used: F115W, F187N, F200W, F335M, F444W, and F470N, which trace the H I Paschen α line, the 3.3 μm PAH band, scattered light and H$_2$S(9) rotational line and CO fundamental rovibrational band, respectively. The observation was designed and processed generally following the procedures outlined in K. M. Pontoppidan et al. (2022). Briefly, a 3×2 mosaic was constructed with 71.5% overlap in rows to produce an image with uniform depth. Each tile was observed using the FULLBOX+6TIGHT dither pattern resulting in a maximum exposure time of 1416–1674 s for the broad and medium-band filters and 2834 s for the narrowband filters. The images were processed using

the JWST calibration pipeline (H. Bushouse et al. 2023) version 11.16.21 with CRDS context `jwst_1077.pmap`. The image resolution at 2.0 μm corresponds to $0\rlap{.}''06$ (or 7 au at the distance of Ophiuchus).

2.2. ALMA

We obtained archival ALMA observations of the VLA 1623 region (project code 2019.1.01074.S;[20] P.I. Maureira) across both Band 6 (217 GHz; G. A. Ediss et al. 2004) and Band 3 (93 GHz; S. Claude et al. 2008). The Band 6 observations were taken on 2021 August 7, October 3, and October 21s in configuration C43-8 for a total of 87 minutes with a phase center of $16^{\rm h}26^{\rm m}26\rlap{.}^{\rm s}42$ $-24°24'30\rlap{.}''00$ (J2000). The observations had a precipitable water vapor (PWV) between 0.8 and 1.5 mm and between 41 and 45 antennas depending on execution. Baseline lengths ranged from 70 m to 11.6 km corresponding to maximum recoverable scale of $0\rlap{.}''85$.

The correlator was set to frequency division mode (FDM) with spectral windows across 216–234 GHz. Pipeline calibration was carried out by the UK ALMA Regional Centre (ARC) node, supplemented by additional self-calibration with CASA (version 6.4.1; The CASA Team et al. 2022). A continuum visibility measurement set was created by combining all channels from the continuum spectral windows with a central frequency of 217 GHz (1.4 mm) and total bandwidth of 5.6 GHz after flagging any channels that may contain strong line emission (although none was apparent). Three rounds of phase-only self-calibration were performed with solution intervals of infinity, 30 s and 18 s, respectively. Model images were created using masks that encompassed strong emission. This resulted in an increase of peak signal-to-noise ratio (SNR) of a factor of $\sim$3. A final round of amplitude self-calibration was attempted but did not result in an improvement of SNR or image fidelity.

The Band 3 observations were taken on 2021 September 7 in configuration C43-9/10 for a total of 85 minutes with a PWV between 3.1 and 3.3 mm and a phase center of $16^{\rm h}26^{\rm m}26\rlap{.}^{\rm s}42$ $-24°24'30\rlap{.}''00$ (J2000). Baseline lengths ranged from 122 m to 16.2 km corresponding to a maximum recoverable scale of $0\rlap{.}''86$ with 49 antennas. The correlator was set to FDM mode with spectral windows across 92–107 GHz. Pipeline calibration was carried out by the UK ALMA ARC node. The central frequency of the final continuum visibility measurement was 93 GHz (3.2 mm) with a bandwidth of 7.5 GHz. As with the Band 6 observations, pipeline calibration was followed by three rounds of phase-only self-calibration (with solution intervals of infinity, 30 s, and 18 s) providing an increase in peak SNR of factor $\sim$4.

For both Band 6 and 3, imaging was performed with `tclean` using Briggs weighting and multiscale, multifrequency synthesis (with scales of 0, 5, 15, and 30 times the synthesized beam). Our fiducial image products, used in the subsequent analyses, have beam sizes of $0\rlap{.}''06 \times 0\rlap{.}''03$ [60°] and $0\rlap{.}''07 \times 0\rlap{.}''05$ [57°] for Bands 6 and 3, respectively (outlined fully in Table A1). Finally, all image products were corrected for the primary beam response using CASA *impbcor*.

2.3. VLA

We carried out observations of the L1688 region with the Karl G. Jansky VLA of the National Radio Astronomy Observatory, using the Q (44 GHz), K (22 GHz), and X (10 GHz) bands (project code 22A-164, P.I. Busquet) with phase centers $16^{\rm h}26^{\rm m}27\rlap{.}^{\rm s}80$ $-24°24'40\rlap{.}''30$, $16^{\rm h}26^{\rm m}25\rlap{.}^{\rm s}63$ $-24°24'29\rlap{.}''4$, and $16^{\rm h}26^{\rm m}24\rlap{.}^{\rm s}60$ $-24°23'37\rlap{.}''00$ (J2000), respectively. The observations were taken across two different epochs (2022 April 2 and 7) with the array in the A configuration and a maximum baseline of $\sim$36 km. Our maximum baseline correlates to a maximum recoverable scale of $1\rlap{.}''2$, $2\rlap{.}''4$, and $5\rlap{.}''3$ for the Q-, K- and X-band observations, respectively. The data was taken using the 3-bit samplers and with two 2 GHz (X-band) and four 2 GHz wide basebands (K and Q bands) and in full polarization.

The data was processed using the VLA Calibration Pipeline[21] within CASA (version 6.5.2). We additionally applied one round of phase-only self-calibration to the Q- and K-band observations, two rounds for the X-band data collected on April 2, and four rounds for the X-band data from April 7. Our model images were created using masks that encompassed strong emission. In both the Q- and K-band observations, we combined spectral windows and scans with an infinite solution interval for the former and down to 90 s for the latter. For both X-band observations, we started with an infinite solution interval (the entire scan) and then down to 96 s for April 2, while for April 7 we went down to 48 s and then 24 s. Self-calibration marginally improved the peak SNR by factors of $\sim$1.2 and 1.5 for the Q- and X-band epochs; however, SNR remained similar for the K-band observations. For the purposes of this work, self-calibration mainly acts to significantly improve the image fidelity for all sources across the respective fields of view by reducing contaminating sidelobes.

As we are combining multiple epoch observations (2022 April 2 and 7), we also must assess the level of variability of each source (discussed in detail in Section 2.3.1). In order to do this, we create images using CASA *tclean* (The CASA Team et al. 2022) from both epochs using the hogbom deconvolver (see, e.g., J. A. Högbom 1974) and a Briggs robust weighting of 2 to maximize sensitivity. The beam sizes of the variability images used in this analysis are $0\rlap{.}''11 \times 0\rlap{.}''1$ [28°] and $0\rlap{.}''11 \times 0\rlap{.}''08$ [8°] for the Q band; $0\rlap{.}''26 \times 0\rlap{.}''14$ [26°] and $0\rlap{.}''2 \times 0\rlap{.}''18$ [17°] for the K band, and $0\rlap{.}''43 \times 0\rlap{.}''19$ [7°] and $0\rlap{.}''42 \times 0\rlap{.}''22$ [6°] for the X band on April 2 and 7, respectively. We present these variability image parameters in Table A1.

For the rest of the analysis within this paper, we make use of fiducial images derived from combining the measurement sets of the 2022 April 2 and 7 observations. For our fiducial VLA 1623 A and B image products, we use a Briggs robust weighting of 0.5 for all VLA frequencies. The fiducial beam sizes for VLA 1623 A and B are $0\rlap{.}''09 \times 0\rlap{.}''06$ [17°], $0\rlap{.}''18 \times 0\rlap{.}''12$ [19°], and $0\rlap{.}''35 \times 0\rlap{.}''16$ [6°] for the Q, K, and X bands, respectively. For VLA 1623 W, we use separate images of the same field using a robust weighting of 2 for the K- and X-band images and a uv-taper of $0\rlap{.}''2$ for the Q-band image. The fiducial beam sizes for VLA 1623 W are $0\rlap{.}''26 \times 0\rlap{.}''14$ [8°], $0\rlap{.}''22 \times 0\rlap{.}''16$ [24°], $0\rlap{.}''42 \times 0\rlap{.}''21$ [7°] for the Q, K, and X bands, respectively. VLA 1623 W is also positioned close to the edge of the primary beam ($\sim$16$''$) in the 44 GHz observations and so naturally has an increased noise level (0.07 mJy beam^{-1})

---

[20] We note here, to avoid confusion, that the ALMA Science Archive incorrectly records the source name as VLA 16293 despite this field covering the position of VLA 1623.

---

[21] https://science.nrao.edu/facilities/vla/data-processing/pipeline

Table 1
Fluxes, Size, and Orientation of Each Object Measured from the ALMA and VLA Observations

Object	Frequency (GHz)	F_{int} (mJy)	σ_{rms} (mJy beam^{-1})	F_{Dust} (mJy)	$f_{Ionized}$ (%)	Deconvolved Size (au)	PA (deg)	Inclination (deg)
VLA 1623 Aa	217	45 ± 5	0.05	45	0.8	14.73 × 8.21 [0.08 × 0.04]	30.9	56
	93	9.0 ± 0.5	0.01	8.7	3.2	13.02 × 6.58 [0.08 × 0.04]	30.8	60
	44	1.2 ± 0.2	0.04	1.0	17.6	11 × 7.1 [1 × 0.5]	15.7	50
	22	0.46 ± 0.05	0.01	0.29	37.3	8.9 × 4.3 [0.8 × 0.3]	172.5	61
	10	0.23 ± 0.05	0.02	0.10	55.9	29 × 8 [7 × 4]	110.8	73
VLA 1623 Ab	217	40 ± 4	0.05	39.6	0.1	13.61 × 6.96 [0.08 × 0.03]	28.2	59
	93	8.8 ± 0.4	0.01	8.7	0.5	12.12 × 6.26 [0.07 × 0.04]	30.1	59
	44	1.2 ± 0.2	0.04	1.2	4.3	10.8 × 5.4 [0.9 × 0.4]	31.5	60
	22	0.44 ± 0.05	0.01	0.38	14.1	10.9 × 4.9 [0.9 × 0.4]	36.2	63
	10	0.12 ± 0.03	0.02	0.04	63.1	…	…	…
VLA 1623 B	217	107 ± 11	0.05	107	0.2	38.8 × 10.89 [0.1 × 0.03]	41.9	74
	93	22 ± 1	0.01	21	0.8	36.7 × 9.08 [0.1 × 0.03]	41.6	76
	44	2.4 ± 0.3	0.04	2.3	6.8	23 × 2.1 [1 × 0.3]	42.5	85
	22	1.0 ± 0.1	0.01	0.9	16.0	25.6 × 1.8 [0.8 × 0.2]	41.5	86
	10	0.35 ± 0.04	0.02	0.19	45.4	26 × 8 [4 × 1]	30.8	71
VLA 1623 W	217	52 ± 5	0.03	51.7	0.1	80.5 × 12.2 [0.8 × 0.1]	10.0	81
	93	8.2 ± 0.4	0.01	8.1	0.9	83 × 11.0 [1 × 0.2]	10.2	82
	44	0.9 ± 0.2	0.07	0.8	11.0	77 × 5 [19 × 2]	8.5	87
	22	0.37 ± 0.05	0.01	0.2	33.9	35 × 18 [3 × 1]	28.8	59
	10	0.24 ± 0.04	0.02	0.08	67.5	35 × 14 [7 × 4]	75.9	66

Note. Integrated fluxes (F_{int}) and local noise level, σ_{rms}, are derived as discussed in Section 3.1.2. Dust fluxes (F_{dust}) and ionized gas fraction (f_{ion}) are derived in Section 3.2.1. All integrated fluxes have been corrected for the primary beam response. Deconvolved disk diameters are derived from the FWHM of our PyBDSF fits with uncertainties in square brackets. We derive inclinations using the ratio of major to minor disk sizes as described in Section 3.1.2.

compared to VLA 1623 AB (0.04 mJy beam^{-1}; see Table 1). However, this does not hinder our analysis. Our fiducial imaging parameters, presented in Table A1, were chosen to provide an optimal trade-off between image fidelity, SNR, and angular resolution. Finally, we correct all images for the primary beam response using CASA impbcor, ensuring accurate fluxes can be measured.

2.3.1. Assessing Variability

Emission at low frequencies ($\lesssim 50$ GHz) from YSOs can be the result of a variety of physical processes; it has been shown to result in variability on short (weeks to months) timescales (see, e.g., G. Pech et al. 2010; S. A. Dzib et al. 2013; H. B. Liu et al. 2014; C. Ubach et al. 2017; A. Coutens et al. 2019). Before combining the VLA observations from the two different epochs (2022 April 2 and 7), we investigated whether there was any significant variation in total flux. We initially imaged the 10, 22, and 44 GHz VLA measurement sets from each date with a Briggs robust value of 2 in order to maximize sensitivity. We then used the Python Blob Detector and Source Finder package (PyBDSF; N. Mohan & D. Rafferty 2015), a Gaussian decomposition algorithm that takes into account the local noise field and any point-spread function effects to accurately determine both the morphology and total flux of sources in interferometric images. Our measured fluxes, extracted from a single Gaussian fit, are reported in Table B1. We then applied the variability criterion from E. Díaz-Márquez et al. (2024), which uses both the rms and calibration uncertainties of the minimum and maximum observed flux as an indication of variability between each epoch, and compares this to the maximum flux deviation. Using this, we found that VLA observations of VLA 1623 Aa, Ab, B, and W can be considered nonvariable to the 3σ level, and so we are able to

combine the measurement sets from each epoch for further imaging.

2.4. Astrometric Alignment

Our use of three different observational instruments necessitated an investigation into the relative astrometric alignment before we could confidently compare their image products. We found that the JWST/NIRCam and ALMA astrometry agreed extremely well, matching object positions on a subpixel scale (e.g., <30 mas). For all data presented here, we rotate the JWST images to the orientation of the ALMA images using the reproject package.[22]

When comparing the ALMA and VLA data, we encountered nonconstant offsets between the positions of objects across the fields, likely induced by the self-calibration process on the VLA data. To correct this, we consider a small box region ($\sim 0\rlap{.}''1 \times 0\rlap{.}''1$) around each object for each consecutive frequency pair considered (e.g., 93 GHz and 44 GHz). We then smooth the image with the smallest beam size to the largest beam size of the frequency pair ensuring a common angular resolution between both images. We fit a 2D Gaussian to both images using PyBDSF and perform an initial shift in the image plane using *scipy.ndimage.shift* to adjust the lower-frequency data to the position reported in the higher-frequency image. We then refine this shift using an image difference minimization processes in which we explore a grid of subpixel shifts around this value, comparing the absolute value of the relative difference between the images. Our final shifts are chosen based on those that minimize the relative differences between the two images (presented in Appendix D). We further check the implemented shift by visually inspecting the overlap

---

[22] https://reproject.readthedocs.io
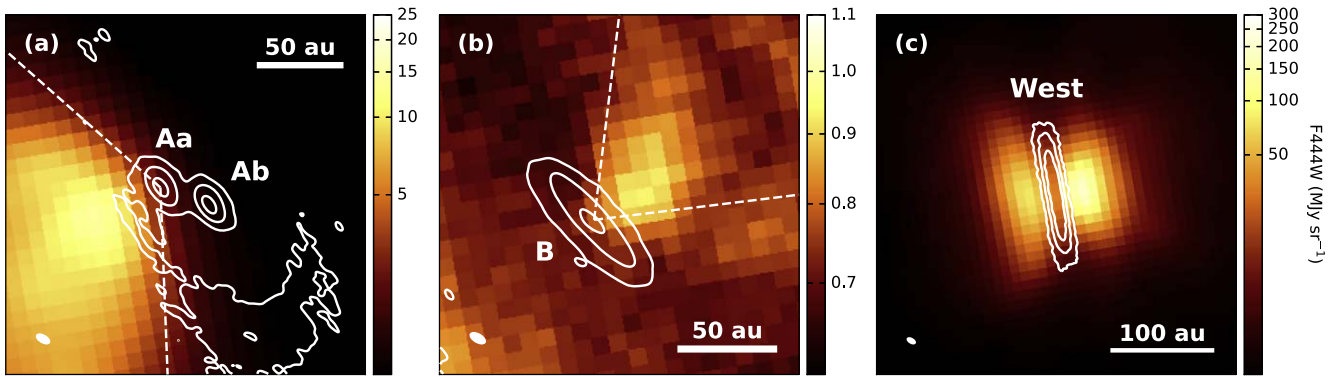
Figure 2. JWST/NIRCam F444W (4.4 μm) images toward VLA 1623 Aa/Ab, B, and W overlaid with ALMA 217 GHz continuum emission (white contours at 8σ, 125σ, 350σ, where σ = 0.02 mJy beam⁻¹). Each panel is peak normalized and shown with a logarithmic stretch. Opening angles of 135° and 75° are shown for reference in panels (a) and (b), respectively.

between the 3σ, 5σ, and 10σ contours of each image to ensure they are cospatial.

3. Results and Analysis

In the following Sections, we discuss the initial results and analysis performed on each of the data sets, and how the observations of each object at different wavelengths compare with one another.

3.1. Morphology and Fluxes

3.1.1. JWST/NIRCam

Due to the highly embedded nature of the VLA 1623 system ($A_V \sim 40$ mag, B. A. Wilking et al. 1989), previous infrared detections of the VLA 1623 AaAb and B protostars were unfeasible. However, due to its separation from AB, VLA 1623 W has been previously detected and appears as a bright infrared source at 4.5 μm and 8 μm (see, e.g., N. M. Murillo & S.-P. Lai 2013; R. Kawabe et al. 2018). We therefore concentrate on the JWST/NIRCam F444W (4.4 μm) images, which are shown in Figure 2.

The brightest emission is detected toward VLA 1623 W, where we see two prominent lobes on either side of a darker lane (traced by the 217 GHz emission) toward the position of the protostellar disk. There is a brightness asymmetry between the two lobes, with the dimmer toward the east, suggesting this represents the far side of the disk that is being partially obscured with respect to the near side. Alternatively, due to the morphology of this asymmetry, the eastern edge may actually be the near side of the disk viewed through a more extincted line of sight. These properties are very similar to observations of scattered light toward other edge-on disks observed in both infrared and millimeter images, for example, Tau 042021 (G. Duchêne et al. 2024). This scattered light emission toward VLA 1623 W originates from high in the disk atmosphere, up to approximately 50 au from the midplane.

Much fainter emission is detected toward both VLA 1623 Aa and B (approximately factors of 10 lower in each case) with an asymmetric conical morphology appearing to originate from close to the central regions of each protostar. The emission morphology seen from VLA 1623 Aa in panel (a) has been previously detected in Spitzer 4 μm images (see, e.g., M. Zhang & H. Wang 2009; N. M. Murillo & S.-P. Lai 2013; R. Kawabe et al. 2018) and aligns with outflows detected in molecular emission lines such as CS(5-4), C₂H

(S. Ohashi et al. 2022), and c-C₃H₂ (N. M. Murillo et al. 2018b) as well as forbidden lines such as [O I] (B. Nisini et al. 2015). This emission is therefore attributed to an outflow cavity. The asymmetry is likely caused by a projection effect as the conical morphology aligns with previously observed, blueshifted, ¹²CO(2–1) emission (see, e.g., C. Hara et al. 2021). Therefore, we are likely seeing the near side of the outflow, which is less extincted than the far side.

In regards to panel (b), this is the first detection of an outflow cavity originating from VLA 1623 B. G. Santangelo et al. (2015) had previously compared their high-velocity CO(2–1) observations with [O I] observations from B. Nisini et al. (2015) and theorized that B may be launching its own jet. We find that the 4.4 μm outflow cavity is aligned with the expected direction of this collimated jet. Furthermore, they theorized that this jet component will be much more compact than the jet associated with VLA 1623 A.

Dashed lines overlaid on panels (a) and (b) in Figure 2 show opening angles of 135° and 75° for VLA 1623 A and B, respectively, fitted by-eye to encompass the observed emission. We report the angle interior to these dashed lines as our estimate for the opening angle of each object. Interestingly, the smaller opening angle of VLA 1623 B corroborates the highly collimated jet hypothesis of G. Santangelo et al. (2015) mentioned above. For both VLA 1623 Aa and B, the 4.44 μm emission appears to be tracing the base of outflowing material along directions perpendicular to the circumstellar disks. Our measured opening angle for VLA 1623 Aa of 135° is significantly wider than outflow opening angles measured from observations of submillimeter molecular line emission (e.g., 20°–30°; W. R. F. Dent et al. 1995; C. Hara et al. 2021). This may be due to the very high sensitivity of the JWST/NIRCam observations, or due to the fact that observations of molecular species only trace specific excitation conditions.

3.1.2. ALMA and VLA

Figure 3 shows the self-calibrated images of VLA 1623 A, B, and W. As in Section 2.3.1, we utilize PyBDSF to measure integrated fluxes, (deconvolved) sizes, and position angles by fitting 2D Gaussians to each object from each image. We also estimate the local noise level, σ_{rms}, using CASA *imstat* by measuring the rms around each object. Finally, we estimate the inclination of each object by considering the ratio of major (θ_{maj}) and minor (θ_{min}) axis sizes at each frequency, i.e., $i = \arccos\left(\frac{\theta_{min}}{\theta_{maj}}\right)$. This inclination calculation assumes the disk
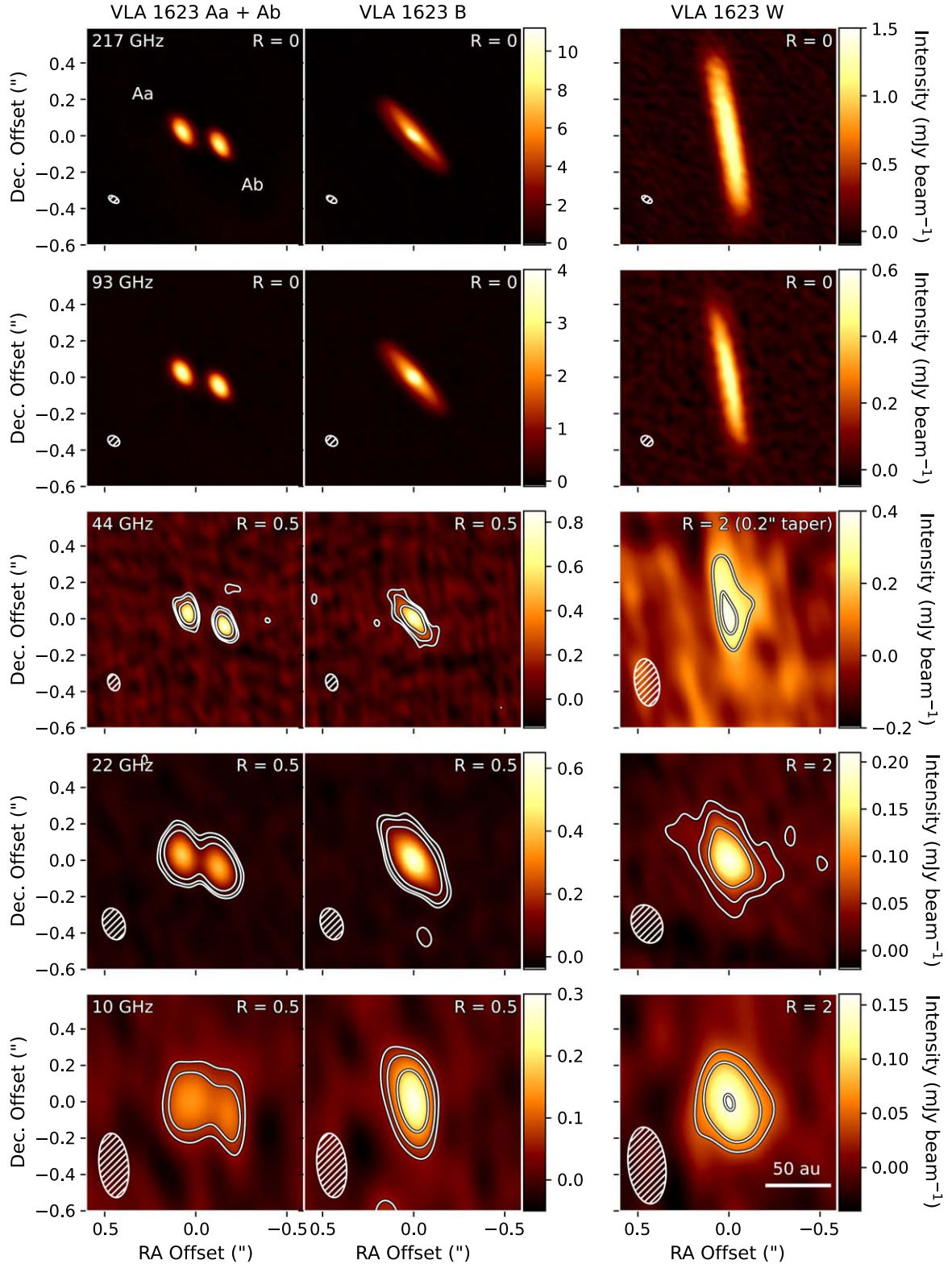
Figure 3. Continuum images of VLA 1623 Aa + Ab (left), B (middle), and W (right). We show 3σ, 5σ, and 10σ contours based on the image rms in white solid lines for all VLA images. The σ values used in each VLA image for each object are shown as the σ_{rms} presented in Table 1. The beam size is shown as the white hatched ellipse in the bottom left of each image. The Briggs robust of each row is shown in the top right of each panel, and the frequency of each row is shown in the top left of each panel in the first column. We additionally indicate a 50 au scale bar in the bottom-right panel, shared across all images.

to be geometrically thin and therefore may underestimate the true inclination. We present all discussed values in Table 1.

Due to the high resolution of our images (0″06–0″4; see Table A1), we manage to successfully resolve VLA 1623 A into its binary components Aa and Ab at all frequencies, although they are only marginally resolved at 10 GHz. By calculating the average difference in peak pixel position of Aa and Ab, we find they are separated by $0″219 \pm 0″003$, or

∼30 au. Since we resolve Aa and Ab at ALMA frequencies and (marginally) at 44 GHz, these are our best insights into the morphological nature of these objects. Both objects share a similar deconvolved position angle of $30°.9 \pm 0°.5$ and $28°.2 \pm 0°.5$ for Aa and Ab, respectively, with a much smaller dust continuum radial extent than their companion B (see Table 1). At 217 GHz, we also partially detect the AaAb circumbinary disk at the 5σ level (see Figure 2(a)), although the scale of the disk (∼$2''.2$; R. J. Harris et al. 2018) is beyond our largest angular scale for this array configuration. This implies that the emission will be filtered, and so we do not analyze this aspect further. The two binary components are morphologically similar across all frequencies except at 10 GHz, where Aa appears to dominate Ab in size/extent. Both objects (Aa, Ab) have similar fluxes across our observations varying on average by around 5% from each other excluding 10 GHz where we see the largest flux difference between the two objects with Aa having almost double the flux of Ab.

We see that the morphology of VLA 1623 B shows indications of being a highly inclined disk ($i = 74°$, Table 1), most notably at 217 GHz, where a dark lane appears to obscure emission from the central source (see Section 3.4 for further discussion). Previous works (see, e.g., R. J. Harris et al. 2018; S. I. Sadavoy et al. 2024) have found similarly high inclination angles for VLA 1623 B. However, at 44 and 22 GHz, this disk structure is much more dominated by a compact 10σ central component with a fainter (3σ) emission surface enclosing the core. VLA 1623 B lies approximately 160 au from the midpoint of Aa and Ab.

VLA 1623 W is located ∼1300 au from VLA 1623 B. This source shows the most significant morphological change across wavelengths with the higher frequencies (217 GHz and 93 GHz) showing an elongation in the north–south direction and the lower frequencies (22 GHz and 10 GHz) dominated by a compact central core. Unfortunately, in our 44 GHz observation, the image fidelity of VLA 1623 W is partially hindered by increased noise due to the object's position at the edge of the primary beam. However, we can still clearly see a compact central component, similar to the other VLA frequencies. We detect a strong compact component at 5σ and a weaker 3σ elongation toward the north similar to the 217 and 93 GHz images, possibly indicating the beginning of a transitional regime dominated by the central star. Additionally, there is a further (tentative, ∼2.5σ–3σ) elongation to the west which is shared by all three VLA observations but not detected at higher frequencies.

3.2. Constructing Millimeter–Centimeter Spectral Energy Distributions

In order to examine the nature of the emission from each object, we construct SEDs across the millimeter- and centimeter-wavelength regimes. To supplement our ALMA and VLA observations, we incorporate ALMA Band 7 (350 GHz) data from R. J. Harris et al. (2018). We take the fluxes reported in R. J. Harris et al. (2018) derived from images with angular resolutions similar to our own (i.e., $0''.14 \times 0''.12$ for AB and $0''.2 \times 0''.17$ for W) to ensure we are tracing emission on similar spatial scales. Further to this, we include additional 6 GHz (C-band) observations from S. A. Dzib et al. (2013). The wide bandwidth of these observations allowed S. A. Dzib et al. (2013) to measure fluxes from the upper and lower sub-bands, providing individual measurements at 7.5 and

4.5 GHz, respectively. It is important to note that VLA 1623 Aa and Ab are not resolved into their binary components at either C sub-band frequency. We therefore consider the fluxes from the upper and lower C sub-bands as an upper limit for both binary components since we do not have any information regarding what share of this flux originates from Aa or Ab. The constructed SEDs for each object are shown in Figures 4 and 5. We summarize the fluxes used in each SED in Table C1.

3.2.1. Quantifying the Dust and Ionized Gas Spectral Indices

Using all fluxes from Table C1, we implement a Markov Chain Monte Carlo (MCMC) approach using *emcee* (D. Foreman-Mackey et al. 2013) to estimate the spectral indices arising from contributions of ionized gas (α_{Ionized}) and dust (α_{Dust}) to the observed flux from our SED. We make use of a double power-law model of the form:

$$F_\nu = A_1\left(\frac{\nu}{10\,\text{GHz}}\right)^{\alpha_{\text{Ionised}}} + A_2\left(\frac{\nu}{10\,\text{GHz}}\right)^{\alpha_{\text{Dust}}}, \quad (1)$$

where F_ν is the flux at frequency ν and A_1, A_2 are the scaling amplitudes. Using this two-component model allows us to decompose the relative contributions of both dust thermal emission (dominant at the highest frequencies in the Rayleigh–Jeans regime) and ionized gas emission (dominant at the lowest frequencies). We use a Gaussian likelihood and flat priors, θ, with the following constraints:

$$P(\theta) = \begin{cases} 1, & \text{if } 0 < A_1 < 1.4. \\ 1, & \text{if } -1.5 < \alpha_{\text{Ionised}} < 1.5. \\ 1, & \text{if } 0 < A_2 < 1.4. \\ 1, & \text{if } 1 < \alpha_{\text{Dust}} < 3.8. \\ -\infty, & \text{Otherwise.} \end{cases} \quad (2)$$

Our amplitudes (A_1, A_2) were loosely constrained through a preliminary least-squares fit using *scipy.curvefit* and by definition must be nonzero. We expect α_{Dust} to vary between ∼3.8 if no dust growth is present (see, e.g., B. T. Draine 2006) and 1.5 in the case of significant dust self-scattering (see, e.g., A. Sierra & S. Lizano 2020). Therefore, we constrain α_{Dust} to lie within the 3.8–1.5 range, ensuring we are probing primarily dust thermal emission. We use the lower limit of α_{Dust} as the upper limit of α_{Ionized} as we want to ensure our value is not tracing the dust thermal emission. We expect ionized gas emission to have typical spectral indices between 0.7 and −0.1 for jets or winds and −0.7 for magnetospheric gyrosynchrotron emission (I. Pascucci et al. 2012; J. J. Condon & S. M. Ransom 2016; G. Anglada et al. 2018), and so we use a generous lower limit of −1.5 for α_{Ionized} to ensure we explore the maximum parameter space.

We use 32 walkers with 2×10^5 steps to sample our distribution and remove a burn-in of 1500 allowing us to determine the α_{Ionized} and α_{Dust} spectral indices as well as their associated uncertainties for each object as shown in Figure 4.

For all objects, we find α_{Dust} values between 2.1 and ∼2.3. VLA 1623 Ab and B have the lowest dust thermal spectral indices of the system with α_{Dust} values of 2.16 and 2.17, respectively. Every object has a very well-constrained α_{Dust} with the highest associated uncertainty being roughly ±0.1. As mentioned previously, α_{Dust} values between 3.8 and 2 indicate that some degree of dust growth may be present in these disks.
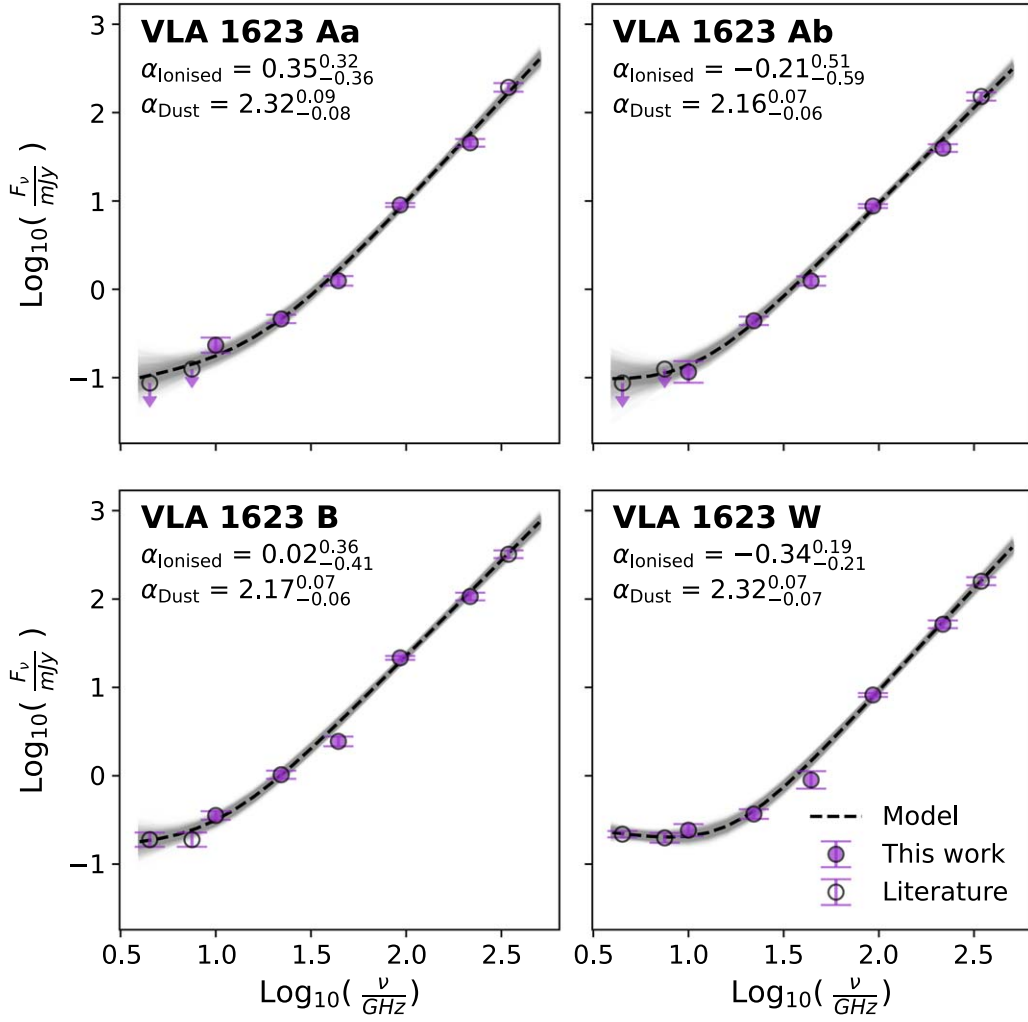
Figure 4. SED of each object overlaid with the models described in Section 3.2.1. Fluxes derived from this work are shown as filled circles, while literature values are shown with open circles. Upper limits are shown as arrows. The shaded region shows random draws from the posterior probability distribution given by the fitting procedure, and the black dashed line indicates the best fit. Each panel also shows the high (α_{Dust}) and low ($\alpha_{\mathrm{Ionized}}$) frequency spectral indices derived from this fit along with their 16th and 84th percentile errors.

The fact that all objects have α_{Dust} values close to 2 also points toward these disks being potentially optically thick.

Considering $\alpha_{\mathrm{Ionized}}$, we find values between -0.35 and 0.4 for all objects. VLA 1623 W has the most negative ionized gas spectral index ($\alpha_{\mathrm{Ionized}} = -0.34$) as well as the lowest uncertainty compared to the other objects. If we consider the uncertainties of the ionized gas spectral index, the minimum $\alpha_{\mathrm{Ionized}}$ of VLA 1623 W (~-0.6) lies close to the expected spectral index for magnetospheric gyrosynchrotron emission (~-0.7; J. J. Condon & S. M. Ransom 2016). However, $\alpha_{\mathrm{Ionized}}$ is also consistent with -0.15 within errors, and thus we may be detecting a combination of optically thin and optically thick ionized gas emission. Additionally, we see a flattening of $\alpha_{\mathrm{Ionized}}$ for VLA 1623 B; however, this only spans the upper (7.5 GHz) and lower (4.5 GHz) sub-bands of the C-band observation and so may hint at a change of regime at longer wavelengths.

We note that in these MCMC runs we have not considered the 4.5 GHz and 7.5 GHz fluxes of Aa and Ab as strict upper limits as the implementation of such constraints within this kind of fitting procedure is nontrivial. Therefore, some of the draws from the posterior distributions violate the upper limits, and the associated negative uncertainties in $\alpha_{\mathrm{Ionized}}$ for these objects are overestimated. Nevertheless, we see that Aa has the highest $\alpha_{\mathrm{Ionized}}$ (0.35) of all objects yet, with a significant error of ± 0.3. This could also indicate either a flat spectral index consistent with zero or a slightly positive spectral index of 0.6–0.7. As discussed in Section 1, a spectral index between -0.1 and 1 may suggest evidence for jet or photoevaporative wind emission. However, an idealized jet is expected to exhibit a spectral index of ~0.6 (S. P. Reynolds 1986). If we consider that the 4.5 GHz and 7.5 GHz observations are an upper limit, then logically, the spectral index must be either positive or flat unless Aa emits significantly at 4.5 GHz.

Considering VLA 1623 Ab, we find that although $\alpha_{\mathrm{Ionised}} = -0.21^{+0.51}_{-0.59}$, the uncertainties are so high that the object could equally fall into all three spectral index regimes—positive, negative, or flat. Once again, using our knowledge that the 4.5 GHz and 7.5 GHz observations are an upper limit, as well as considering that Ab has approximately half the flux of Aa in the X band, it is not unlikely that it is similarly weaker at frequencies $\lesssim10$ GHz, and therefore the true spectral index may be higher than what we report here.

Finally, we can correct our measured fluxes for contaminating emission by using the ionized gas and dust thermal
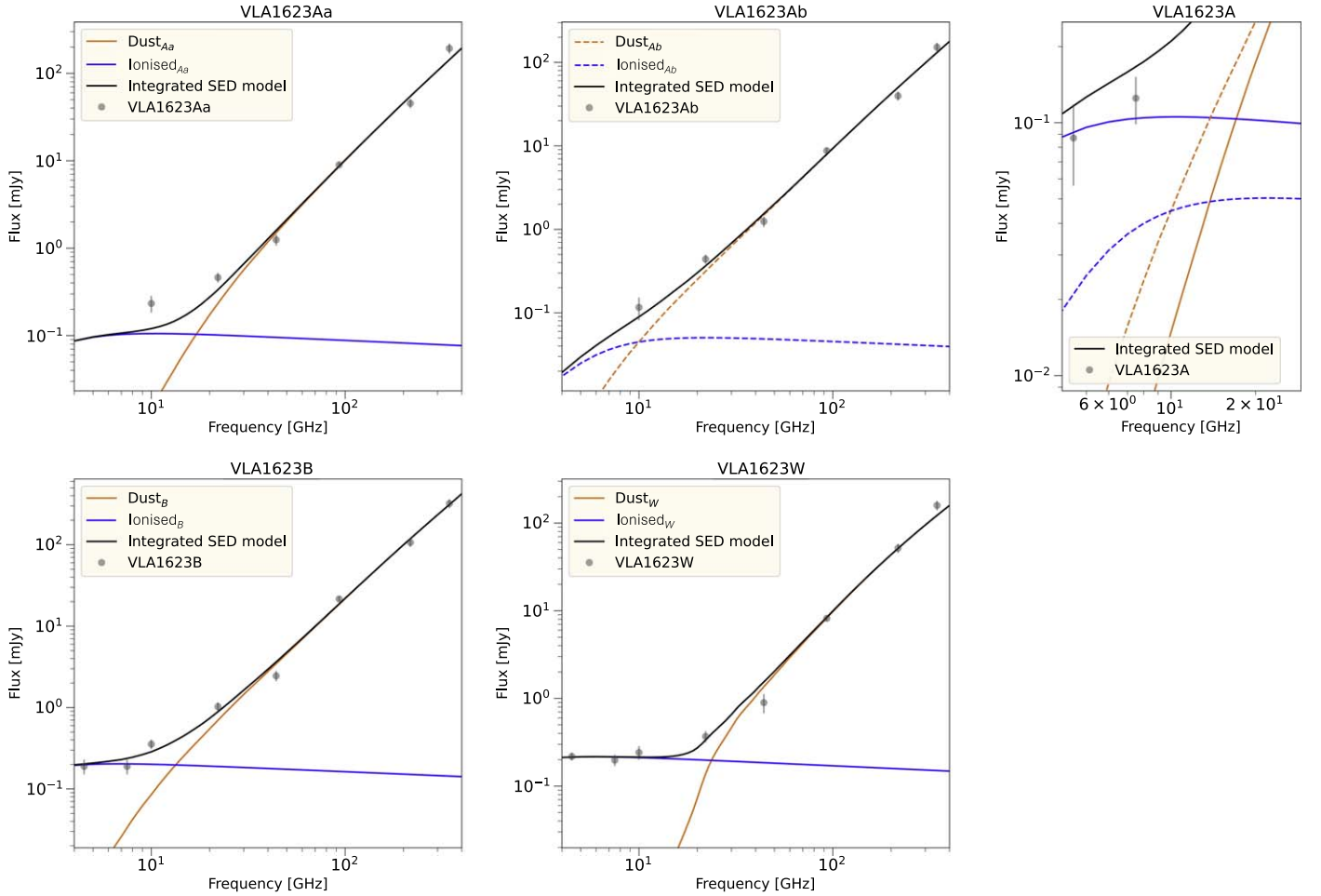
Figure 5. Top: SED models for the VLA 1623 Aa and Ab resolved, integrated fluxes alongside the combined model, A, for the unresolved *C*-band data (S. A. Dzib et al. 2013). Symbols show the observational data, colored lines show the SEDs of individual emission components in our model (Table 2). For clarity, we show the Aa emission components as solid lines and Ab components as dashed lines in the combined model. Integrated flux densities are shown in black lines. Bottom: same as the top but for resolved observations of VLA 1623 B and W, respectively.

components of our SED fit to estimate the uncontaminated flux from thermal dust emission. To determine this, we evaluate Equation (1) assuming the dust thermal component has no contribution (i.e., $A_2 = 0$) to estimate our ionized gas flux and subtract this from our integrated fluxes. We call this contaminant-corrected flux the dust flux, F_{Dust} and include it in Table 1 along with an estimate of the fraction of ionized emission, f_{Ionized}, compared to the total integrated flux, F_{int}.

3.2.2. Reproducing the Observed SEDs with Combinations of Dust and Ionized Gas

In addition to the dust and ionized gas spectral indices of these objects, we can attempt to model the underlying population of dust and nature of the ionized gas mechanisms that create the resultant SEDs. Unfortunately, we do not have sufficient spatial resolution for frequencies $\lesssim 22$ GHz to accurately describe the morphology of the dust disk for each object across our entire data range. In addition, in Class 0/I objects, a number of case studies have shown that in the high-density regions traced by VLA observations, the thermal structures may be complicated due to viscous heating (H. B. Liu et al. 2019; H. B. Liu 2021; J. Zamponi et al. 2021; W. Xu 2022; W. Xu et al. 2023; S. Takakuwa et al. 2024). Therefore, instead of the commonly adopted approach

of fitting a passive disk model (e.g., E. I. Chiang & P. Goldreich 1997), we follow the approach of H. B. Liu et al. (2019) and H. B. Liu et al. (2021) to model the spatially unresolved SED with components of dust and ionized gas emission. For simplicity, we assume that the physical properties within each of these emission components are uniform.

Since the dust emission in our objects may be optically thick at these frequencies (discussed in Section 3.2.1), the formulation needs to take into account the mutual obscuration of the emission components. For each source, the integrated flux density is expressed by

$$F_\nu = \sum_i F_\nu^i e^{-\sum_j \tau_\nu^{i,j}}, \qquad (3)$$

where F_ν^i is the flux density of the dust or ionized gas emission component i, and $\tau_\nu^{i,j}$ is the optical depth of the emission component j to obscure the emission component i.

When considering the contribution of ionized gas emission, we can use the analytical expression of F_ν^i and $\tau_\nu^{i,j}$, which depends on three free parameters: the electron temperature (T_e), the emission measure (EM), and the solid angle (Ω_{ff}) and is provided in Appendix E.1. Since we do not possess sufficient independent measurements at low frequencies to fully constrain

Table 2
Model Parameters

Component	T (K) (1)	Ω[a] (10^{-12} sr) (2)	Σ_{dust} (g cm^{-2}) (3)	a_{max} (mm) (4)	EM (cm^{-6} pc) (5)	M_{dust} $M_\oplus$ (6)
VLA 1623 Aa						
Dust	218^{+90}_{-43}	$0.24^{+0.066}_{-0.072}$	$4.5^{+1.8}_{-1.3}$	$17^{+10}_{-6.0}$	⋯	28^{+22}_{-14}
Ionized gas	8000	$4.3^{+3.4}_{-1.6} \cdot 10^{-2}$	⋯	⋯	$2.98^{+2.15}_{-1.53} \cdot 10^7$	⋯
VLA 1623 Ab						
Dust	236^{+95}_{-63}	$0.20^{+0.08}_{-0.06}$	$20^{+14}_{-8.4}$	$19^{+15}_{-9.9}$	⋯	113^{+82}_{-45}
Ionized gas	8000	$4.6^{+6.2}_{-2.5} \cdot 10^{-3}$	⋯	⋯	$1.5^{+1.8}_{-1.1} \cdot 10^8$	⋯
VLA 1623 B						
Dust	113^{+48}_{-29}	$1.1^{+0.40}_{-0.34}$	$23^{+15}_{-9.1}$	$15^{+14}_{-8.9}$	⋯	650^{+810}_{-380}
Ionized gas	8000	$0.20^{+0.14}_{-0.079}$	⋯	⋯	$1.2^{+0.97}_{-0.54} \cdot 10^7$	⋯
VLA 1623 W						
Dust	$25^{+5.5}_{-4.5}$	$2.6^{+0.79}_{-0.60}$	$6.7^{+13}_{-5.0}$	$2.8^{+7.2}_{-1.4}$	⋯	448^{+1300}_{-360}
Ionized gas	8000	$0.28^{+0.14}_{-0.082}$	⋯	⋯	$8.8^{+4.6}_{-3.2} \cdot 10^6$	⋯

Notes. Column: (1) Dust temperature for dust emission components and electron temperature for ionized gas emission component. Column: (2) Solid angle of the emission components. Column: (3) Dust column density. Column: (4) Maximum dust grain size. Column: (5) Emission measure for the ionized gas emission component. Column: (6) Dust mass in units of Earth masses ($M_\oplus$).
[a] 1 sr $\sim 4.25 \times 10^{10}$ square arcsecond.

these three parameters, we nominally assume $T_e = 8000$ K for all ionized gas emission components in our models.

To accurately model the dust emission within circumstellar disks, we must consider the effect of dust scattering (A. Kataoka et al. 2015; H. B. Liu 2019; Z. Zhu et al. 2019), and so to incorporate this into our model, we use the DSHARP dust opacity and Equations (10)–(20) presented in T. Birnstiel et al. (2018) when modeling the dust emission components, which has previously been applied to Class 0 and Class I YSOs (see, e.g., S. Takakuwa et al. 2024; O. M. Guerra-Alvarado et al. 2024). Specifically, for dust components that have temperatures below 170 K, we assume that they are coated with water ice and use the DSHARP-default opacity table, which assumed that the dust grains are composed of water ice (S. G. Warren 1984), astronomical silicates (B. T. Draine 2003), troilite, and refractory organics (T. Henning & R. Stognienko 1996; see Table 1 of T. Birnstiel et al. 2018). For dust components with temperatures >170 K, we use the corresponding DSHARP opacity for ice-free grains. The adopted sublimation temperature of 170 K is motivated by the dependence of volatile sublimation on local gas pressure (S. Okuzumi et al. 2016; see their Equations (3) and (4)). Previous studies have typically used sublimation temperatures in the range of 150–170 K (e.g.,160 K; J. J. Tobin et al. 2023). However, due to the comparatively higher densities associated with Class 0/I objects, we choose the higher end of the temperature range. Further to this, it is assumed the dust grains are morphologically compact (i.e., low porosity), consistent with recent ALMA observations (e.g., R. Tazaki et al. 2019).

The size-averaged dust opacities were evaluated by assuming a power-law grain size (a) distribution $n(a) \propto a^s$ with $s = -3.5$ between the minimum and maximum grain sizes (a_{min}, a_{max}; i.e., $n(a) = 0$ elsewhere), which are insensitive to the value of a_{min}. We artificially set $a_{min} = 0.1\ \mu$m, which is common in the studies of protoplanetary disks (e.g.,

C.-Y. Chung et al. 2024). The remaining free parameters for each dust emission component are dust temperature (T_{dust}), dust column density (Σ_{dust}), solid angle (Ω_{dust}), and a_{max}.

Using the assumptions and parameters above, we model both dust and ionized gas contributions to the SED of each object with an MCMC approach, again, using emcee. We incorporate flat priors, allowing each parameter to increase or decrease by 1 order of magnitude. When considering VLA 1623 Aa and Ab, we fit the resolved 217–10 GHz SED individually. However, for the 7.5 GHz and 4.5 GHz observations, we use the integrated SED from both Aa and Ab models, as these objects are unresolved at these frequencies. Our MCMC fitting used 300 walkers with 5×10^4 steps and removed a burn in of 1×10^4, allowing us to fully probe the parameter space. We present our best-fit parameters and their respective uncertainties in Table 2 as well as the resulting model SEDs in comparison to the observations in Figure 5.

Using a single dust population, we find that all objects are consistent with a maximum grain size >1 mm. This result corroborates the findings of Section 3.2.1, where α_{Dust} has values between 3.8 and 2 for all objects, which can be explained by the presence of grain growth in the circumstellar disk (see, e.g., B. T. Draine 2006). While these values are rather unconstrained, they represent the necessity of large dust grains in order to replicate the observed SED at low frequencies. This is particularly pertinent due to our inclusion of ionized gas in the model, which contributes significantly at low frequencies (S. A. Dzib et al. 2013). Therefore, we require not only contributions from the ionized gas, but also from large, hot dust grains.

Nevertheless, we find several issues arise from employing the single dust population and ionized gas model. For example, the Σ_{dust} and a_{max} have to have high values in order to reproduce the observed low spectral indices at ~10–50 GHz. The very high a_{max} values here are not consistent with the

previous detection of the 872 μm polarization due to dust self-scattering in these sources (R. J. Harris et al. 2018). Furthermore, in all four sources, the single dust component model cannot reproduce both the low spectral indices at ~10–44 GHz and the high spectral indices at 217–350 GHz simultaneously.

For a better explanation of the observational data, it is plausible to consider the next level of complexity by including more emission components and the mutual obscuration of these components. A natural way to replicate the more optically thick spectral indices (~2) for frequencies $\gtrsim$22 GHz without contributing too much flux at ~6 GHz, is to include another dust emission component that has a high a_{max} value and a high temperature, which is obscured at $\gtrsim$30 GHz. This may indicate dust mass segregation or dust growth, which have been previously observed in Class 0/I protoplanetary disks (see, e.g., I. Han et al. 2023).

For all four sources, the discrepancy between model and data at $\gtrsim$200 GHz can be amended by including a relatively optically thin dust emission component. Unfortunately, the a_{max} of this relatively optically thin dust emission component cannot be constrained by the present data. However, previous detections of dust self-scattering at 872 μm indicate that the a_{max} of these relatively optically thin dust components are of the order of ~100 μm.

Finally, we find our single dust population models to be quite unconstrained as the SEDs of the observed sources need to be represented by mixtures of optically thick and thin dust and ionized gas emission. We discuss qualitative models using multiple, mutually obscuring dust populations in Appendix E.2 while appreciating the caveat that the inclusion of these components further adds to the degeneracy. The derived overall dust masses in these sources for the single dust model are of the order of tens to hundreds of $M_\oplus$. However, it is important to note that the models with single and multiple dust components do not indicate qualitatively different overall dust masses. The major uncertainties in the dust mass estimates originate from the assumed dust opacities.

3.3. Pixel-by-pixel Spectral Index Maps

Further to the disk integrated spectral indices discussed in Sections 3.2.1 and 3.2.2, we are able to probe any spatial variations in the spectral index across individual pixels by comparing images at consecutive frequency pairs for each object. We calculate the spectral index on a per-pixel basis, after smoothing each image to the larger of the beam sizes for each pair of adjacent frequencies in the ALMA and VLA data sets (e.g., from 217–10 GHz). We show the results of these calculations in Figure 6.

Examining the 217–93 GHz spectral index ($\alpha_{217-93\,GHz}$), we see all objects share a similar spectral index gradient. The general trend of decreasing spectral index from ~2.5 to $\lesssim$2 toward the center of the emission is shared across all objects, likely indicating an optical depth increase caused by high densities near the central protostar. A similar overall trend appears in the 93–44 GHz spectral index ($\alpha_{93-44\,GHz}$) for A and B with an increased value of ~3 in the outer regions which decreases to ~2.5 close to the center. In addition, we find that generally $\alpha_{93-44\,GHz} > \alpha_{217-93\,GHz}$ for all objects indicating a possible reduction in the optical depth at these lower frequencies.

This combination of optically thick emission for 217–93 GHz and more optically thin emission at 93–44 GHz corroborates our SED analysis of the spectral index (see Section 3.2.1), where we find α_{Dust} to be just above ~2. This can be explained by multiple populations of optically thick and optically thin dust emission components with mutual obscuration, which we discuss in detail in Appendix E2.

All objects exhibit much lower spectral indices, typically $\leqslant$2, for frequency pairs $\leqslant$44 GHz. The reduction in spectral index for all objects is correlated with an increased fraction of ionized flux (see Table 1) with the lowest spectral indices associated with the 22–10 GHz frequency pair. Considering this, alongside our spectral index SED analysis in which all objects had $\alpha_{Ionized} < 0.5$, we infer that all objects in this system are subject to ionized gas emission, which contributes significantly to observations below 44 GHz.

VLA 1623 W exhibits a unique morphology compared to the other objects in the system for frequencies <93 GHz. For $\alpha_{93-44\,GHz}$ we see a decreasing east–west gradient in comparison to the radial gradients seen in A and B. This may be an effect of projection and optical depth whereby the eastern edge is nearest the observer and thus has a higher column density compared to the western side, as mentioned in Section 3.1.1.

Additionally, in VLA 1623 W, we see $\alpha_{44-22\,GHz} \sim 0.7$ in the very central regions indicating emission from a non-dust component close to the center of the disk. The spectral index continues to decrease for $\alpha_{22-10\,GHz}$, which is <1 for the entire emission region. Finally, it is worth noting the two lobes of particularly low spectral index (~0.4) in the east and west perpendicular to the dust disk. There is also tentative evidence of low spectral index extensions to the west seen in the 93–44 GHz and 44–22 GHz spectral index maps.

3.4. The Millimeter Continuum Emission Surface in VLA 1623 B

Examining our 217 GHz observations of VLA 1623 B in detail reveals an interesting morphology. The high resolution of the observations (and the favorable beam orientation along the disk minor axis) means that all of the emission is extremely well resolved. While emission along the disk major axis appears to be symmetric, there is an obvious asymmetry along the minor axis with brighter emission toward the northwest, and a "dark lane" running along the near side of the disk (see Figure 7). We note that the near- and far-disk sides as seen at 217 GHz are in agreement with the jet direction shown by SO and SiO emission in C. Codella et al. (2024), i.e., blueshifted in the northwest direction and redshifted in the southeast direction.

To quantify the vertical extent of the millimeter continuum emission in the VLA 1623 B disk, we use the GoFish package (R. Teague 2019) to overlay an emission surface that best matches the observed morphology. This takes the form of a flared disk with an outer taper following the parameterized form

$$z(r) = z_0 \left(\frac{r}{1''} \right)^\psi \exp\left(\frac{-r}{r_{taper}} \right)^{q_{taper}}, \qquad (4)$$

where z_0 is the emission surface at a reference radius, r is the deprojected radius, r_{taper} is the radius of the taper, and the exponents ψ and q_{taper} determine the slope of emission surface
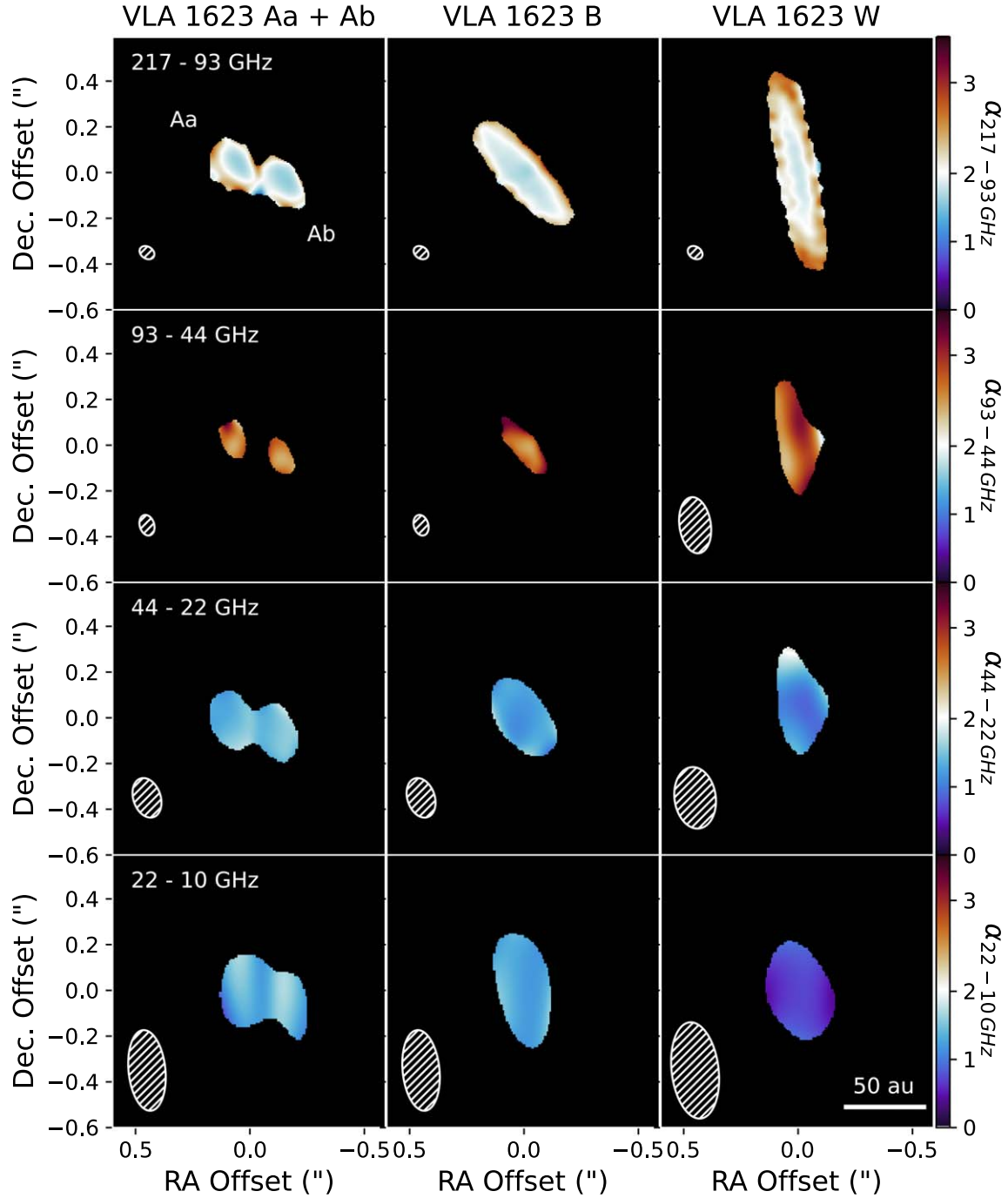
Figure 6. Spectral index maps for each object and each adjacent frequency pair. For B and W, we center each image on the peak pixel of the object in the highest-frequency continuum image, and for Aa and Ab, we center the image on the binary midpoint. We show a 50 au scale bar, which is shared across all images. We show the common beam for both frequency bands in the bottom-left corner as a white ellipse. All images use a 5σ mask where $\sigma = \sigma_{\mathrm{rms}}$ in Table 1 except for VLA 1623 W, which for 93–44 GHz and 44–22 GHz, uses a 3σ due to the weak detection at 44 GHz. All images share a common divergent color bar centered on $\alpha = 2$.

in the inner and outer disk, respectively. We experimented with a variety of surface morphologies and found that the observations appear to be well matched by-eye with $z_0 = 0\rlap{.}''5$, $\psi = 1.1$, $r_{\mathrm{taper}} = 0\rlap{.}''23$ (32 au), and $q_{\mathrm{taper}} = 2.0$, the model of which is shown overlaid on the observations in Figure 7(c). This emission surface varies in terms of the relative height traced throughout the disk, but ranges from $z/r = 0.25$ to 0.35 depending on radius. This suggests the $\tau = 1$ surface for these frequencies in this disk is located high above the midplane, and is further evidence for the optically thick nature of the disk. In fact, the surface is located at similar heights to the disk regions traced by CO isotopologues observed toward Class II disks (C. J. Law et al. 2023), and such a morphological similarity is seen between the gas and dust in other Class 0 disks, for example, in the CAMPOS survey (C.-H. Hsieh et al. 2024). Determining the precise origin of the extremely flared dust morphology requires dedicated radiative transfer modeling of multiwavelength observations, which we will perform in a future study (I. C. Radley et al. 2025, in preparation).
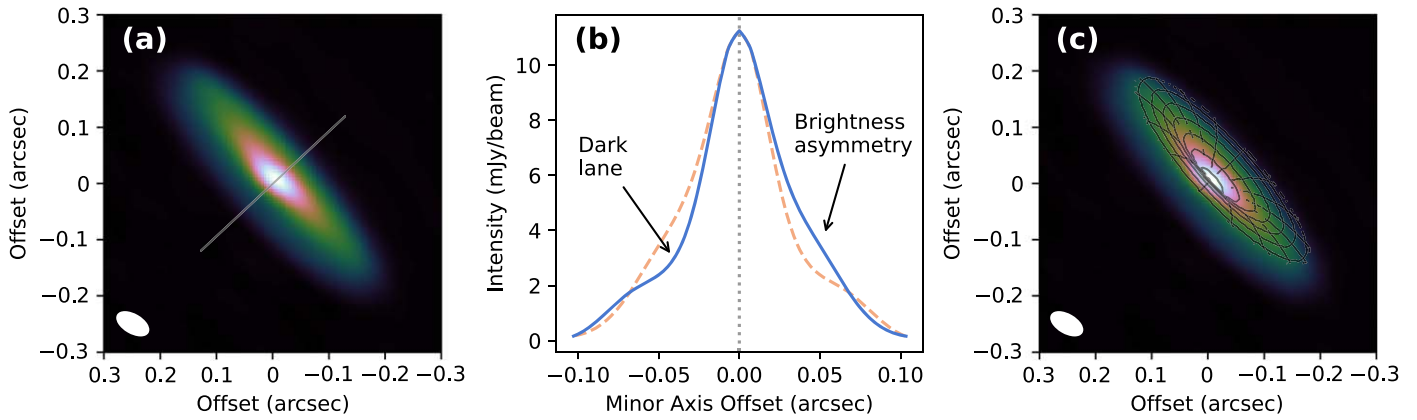
Figure 7. (a) Zoom-in of the 217 GHz ALMA image of VLA 1623 B shown with a color map to highlight faint features. The gray line denotes a cut across the minor axis of the disk. (b) Intensity along the minor axis cut from panel (a) compared with a mirrored profile (dashed line). There is a dark lane on the southeastern side and brightness asymmetry on the northwestern side of the disk detected at a high significance (the rms of 0.02 mJy beam^{-1} is smaller than the line thickness). (c) The same as panel (a) but overlaid with a representative surface model at relative heights of $z/r \sim 0.3$ (see the text). These features demonstrate the extremely flared nature of the millimeter continuum emission, suggesting that larger grains are vertically well-mixed in the disk.

4. Discussion

4.1. The Unsettled (and Unstable?) Young Disk of VLA 1623 B

Our high-resolution observations at 217 and 93 GHz reveal an inclined ($\sim 74°$) disk morphology for VLA 1623 B with significant flaring seen in the 217 GHz continuum that is much less prominent at 93 GHz. In Section 3.4, we use our 217 GHz observations to determine a $z/r \sim 0.3$ in the inner regions of the disk, and 0.2 in the outer (>30 au) regions. Such a morphology is reminiscent of observations of highly inclined Class II protoplanetary disks at visible and infrared wavelengths, in which the brightest emission is the result of scattering of stellar light by dust grains at high relative heights in the disk atmosphere (see, e.g., H. Avenhaus et al. 2018; G. Duchêne et al. 2024). Similarly high flaring angles and/or dark lane asymmetries have also been observed in other Class 0 and I disks (see, e.g., IRAS 04302+2247, Z.-Y. D. Lin et al. 2023; R CrA IRS7B-a, S. Takakuwa et al. 2024; IRAS4A1, O. M. Guerra-Alvarado et al. 2024). One explanation for these features is that vertical dust settling may occur primarily between the Class I and II stages (see, e.g., N. Ohashi et al. 2023), which would explain the more geometrically thin disks found for Class II objects (e.g., C. Pinte et al. 2016). Alternatively, the suspension of dust grains in the upper disk layers may be due to physical mechanisms operating within young disks.

One such mechanism may be potential gravitational instability operating within the disk of VLA 1623 B. Gravitational instability can trigger spiral shocks in the disk, which have been shown to result in significant increases in vertical mixing and turbulence (see, e.g., A. C. Boley & R. H. Durisen 2006). Such behavior would act to lift dust grains that might normally be settled toward the midplane into the upper layers of the disk, resulting in an unsettled disk as observed here. Class 0 and I protoplanetary disks are deeply embedded, and as such, they are expected to be more dynamically unstable than Class II disks due to their increased disk-to-star mass ratio (E. I. Vorobyov & S. Basu 2006; Y. Tsukamoto et al. 2017). To accurately calculate the disk-to-star mass ratio, we require high-resolution gas observations of the inner regions of protoplanetary disks. Recent radiative transfer models focusing on $C^{17}O$ kinematic observations have constrained the protostellar mass of VLA 1623 B to be $1.9\,M_\odot$

(S. I. Sadavoy et al. 2024). This tracer is less subject to contamination from infalling envelopes or streamers and thus provides a robust estimate of the stellar mass.

A disk-to-star mass ratio $\geqslant 0.1$ indicates that the disk's self gravity may be important and thus influence further evolution of the system (K. Kratter & G. Lodato 2016). If we use the disk dust mass of $650\,M_\oplus$ derived in Section 3.2.2 and a standard 1:100 dust-to-gas mass ratio, we estimate a disk-to-star mass ratio of ~ 0.1 which implies that the disk may be gravitationally unstable. It is important to note that our observations at 217 GHz and potentially at 93 GHz are optically thick due to high densities and a high inclination. This means we are only tracing the $\tau_\nu \sim 1$ emission surface (C.-Y. Chung et al. 2024; L. Delussu et al. 2024) and so our disk mass and therefore disk-to-star mass ratio is likely to be a lower limit. With this consideration, we believe it is very likely that the disk is gravitationally unstable.

Alternatively, the lack of settling may arise from infalling material, which can significantly perturb the disk and excite instabilities such as spiral waves entraining dust grains into spiral arms (e.g., J. Bae et al. 2015). VLA 1623 B has been observed to have wide line widths in SO ($>10\,km\,s^{-1}$; C.-H. Hsieh et al. 2020) believed to originate from shocks caused by infalling material. Additionally, in the presence of anisotropic infall, the models of A. Kuznetsova et al. (2022) found a mean dust disk diameter of ~ 55 au which is slightly larger than the dust disk we derive for B at 217 GHz (~ 40 au). However, since this model focuses on higher-mass cores, we would expect this to be lower in low-mass objects, such as VLA 1623 B. Therefore, infall may have a significant impact on the circumstellar disk of VLA 1623 B.

Nevertheless, if the disk of VLA 1623 B is unstable, due to gravitational instability or infall, then we would expect the manifestation of axisymmetric structures such as spiral density waves (L. Mayer et al. 2004; J. Bae et al. 2015; J. Huang et al. 2018), which are not observed. However, as the disk is optically thick at 217 GHz, we are not tracing through all layers of emission, and thus any existing substructures may remain hidden (see, e.g., W. Xu 2022). Alternatively, Y. Tsukamoto et al. (2017) found that spirals induced by GI may be short lived and only persist for 10% of the Class 0/I disk's lifetime. If the disk contains nonaxisymmetric structures, we would require further observations at a more optically thin frequency

that matches or improves upon the resolution of our 217 GHz observation. With currently available instrumentation, this would present a challenge.

4.2. Environmental Impact on Disk Evolution

C.-H. Hsieh et al. (2024) performed an ALMA Band 6 (217 GHz) survey probing the effect of evolutionary state and star-forming environment on the observed protostellar disk radii. Using similarly high-resolution observations ($\sim 0\rlap{.}''1$), they found dust disks in Ophiuchus to have an average radii of 35 au and 26 au for Class 0 and I objects, respectively, meaning that Ophiuchus YSOs have a smaller average dust disk radii than Serpens (77 au and 49 au) and Aquila (50 au and 62 au), for example (C.-H. Hsieh et al. 2024). We find that VLA 1623 W has a circumstellar dust disk radius of 40.3 ± 0.4 au, which aligns with previous 217 GHz observations (e.g., 48 au; S. Mercimek et al. 2023). This radius is therefore just under double the average Class I dust disk radius of Ophiuchus as a whole, and it is significantly larger than the other members of the VLA 1623 system. We see that VLA 1623 B is roughly half the size of VLA 1623 W at 19.4 ± 0.1 au corroborating previous estimations of the dust disk size at 217 GHz (see, e.g., 23 au, R. J. Harris et al. 2018; 22 au, S. Mercimek et al. 2023). However, as mentioned in Section 4.1, the small size of VLA 1623 B may be due to the influence of infalling material perturbing the disk evolution (e.g., A. Kuznetsova et al. 2022).

The most extreme difference is seen in the VLA 1623 Aa and Ab circumstellar dust disks, which have radii of 7.37 ± 0.04 au and 6.81 ± 0.04 au, respectively, making them roughly one-fifth the size of the average Class 0 population in Ophiuchus. However, small protostellar dust disks are not uncommon for binary systems (see, e.g., F. Long et al. 2019; C. F. Manara et al. 2019; S. Narayanan et al. 2023) and may be caused by disk truncation through binary interaction if Aa and Ab are close enough to interact with each other (see, e.g., P. Artymowicz & S. H. Lubow 1994).

It appears that in comparison to the overall population of Ophiuchus, VLA 1623 Aa, Ab, and B have significantly smaller radial extents, whereas VLA 1623 W has a significantly larger radial extent. Recent ALMA-FAUST images of $C^{18}O(2–1)$ (S. Mercimek et al. 2023) revealed streamers that extend up to 1000 au, spatially and kinematically connecting the envelope and outflow cavities of the A1 + A2 + B system with the disk of VLA 1623 W. The presence of the streamers, as well as the spatial (1300 au) and velocity (2.2 km s^{-1}) offsets of VLA 1623 W, suggests two main scenarios: either the sources W and A + B originated in separate cores and have interacted with each other (as suggested by S. I. Sadavoy et al. 2024), or source W was expelled from the VLA 1623 multiple system while it was forming. In the latter case, the streamers could channel material from the envelope and cavities of VLA 1623 A + B toward VLA 1623 W, thereby contributing to the determination of its ultimate mass and chemical composition (S. Mercimek et al. 2023).

4.3. Evidence for Jet Emission

Protostellar objects are often associated with jets, outflows, and disk winds (see, e.g., E. Macías et al. 2016). Winds and jets can exhibit very similar spectral indices and thus require further investigation, often using morphological arguments to discern

which mechanism is in operation (G. Anglada et al. 2018). Here we examine whether our VLA observations reveal the presence of any such phenomena in the members of VLA 1623.

4.3.1. VLA 1623AB

VLA 1623 Aa and Ab have both been associated with their own molecular outflows (e.g., C. Hara et al. 2021), which necessitates a launching mechanism such as a protostellar jet or a disk wind (see T. P. Ray & J. Ferreira 2021; I. Pascucci et al. 2023, for reviews). Through our SED analysis, we found that both objects exhibit a significant ionized gas contribution at low frequencies (>50% at 10 GHz). Considering the upper limit caveats at low frequencies for Aa and Ab, we note that both objects have an integrated spectral index consistent with a thermal radio jet (G. Anglada et al. 2018).

We find an indication of jet-like behavior for Aa at 10 GHz, where we see a sudden increase in the flux and size of Aa compared to Ab, which is accompanied by an extension with a position angle of $110° \pm 20°$. The extension is perpendicular to the position angle of the dust disk derived at 217 GHz, $30\rlap{.}°9 \pm 0\rlap{.}°5$, as would be naively expected from jet emission (G. Anglada et al. 2018). If the emission is arising from a jet or a wind, then the emission region must be at sub-beam scales (<20 au), which supports either the disk launching theory proposed in S. Ohashi et al. (2022) at a radius of ~ 5–16 au or is evidence of a protostellar jet.

Further to this, using CS observations, S. Ohashi et al. (2022) traced the origin of the outflow associated with the VLA 1623 A binary to a position close to Aa but could not definitively determine the true launch site due to low spatial resolution. Additionally, C.-H. Hsieh et al. (2024) postulates that the misalignment of the Aa and Ab outflows detected in C. Hara et al. (2021) could be explained by an outflow launched by B, which is misaligned to the VLA 1623 A binary.

In Figure 2(b) we see an outflow cavity that is cospatial with the 217 GHz continuum of VLA 1623 B. As discussed in Section 3.1.1, this outflow cavity is aligned with the expected position angle of a highly collimated jet predicted by G. Sant-angelo et al. (2015). Unlike VLA 1623 Aa, we do not detect a perpendicular emission component at 10 GHz. However, as the jet is expected to be highly collimated, which may also explain the smaller opening angle (75°) compared to Aa (135°), the launching region may also occupy a much smaller spatial extent.

The proximity of the conical emission in our JWST NIRcam data (see Figures 2(a) and 2(b)) to Aa and B point toward both objects driving individual outflows. This result confirms the previous hypotheses of C.-H. Hsieh et al. (2020) and S. Ohashi et al. (2022). Furthermore, due to the increased flux and perpendicular PA at 10 GHz for Aa, we believe these observations suggests that Aa is more likely to be the origin of the large-scale outflow.

There are two possible solutions to improve our understanding of these objects. First, we can use time-series observations to probe variations in the 10 GHz flux, which we attribute primarily to changes in the contribution of ionized gas. Second, we may benefit from increased integration times and therefore sensitivities to pick up on any fainter emission that may arise if Ab has different jet properties to Aa.

4.3.2. VLA 1623 W

VLA 1623 W has not been associated with a jet or an outflow in previous studies, possibly due to its low flux and the previous ambiguity of its nature (e.g., C. Hara et al. 2021; S. Mercimek et al. 2023). In contrast, through our SED fitting, we find a negative integrated spectral index at low frequencies ($<10\,\text{GHz}$), which is not seen in any other object in the VLA 1623 system. We also see a general trend of decreasing spectral index with decreasing frequency in both the integrated and pixel-by-pixel spectral indices as well as an increased contamination fraction at 10 and 22 GHz. This indicates significant ionized gas emission dominates at lower frequencies, which is similarly found in other Class I disks (see, e.g., IRAS 04302+2247; M. Villenave et al. 2023).

At 44 GHz, we see evidence of a tenuous ($\sim 2.5\sigma$–3σ) extension perpendicular to the plane of the disk, which coincides with a low $\alpha_{93-44\,\text{GHz}}$ value in the spectral index map. We note that this extension is at the noise level, and the spectral index map may be subject to edge effects. However, at 10 GHz and 22 GHz, we see similar extensions (although not perfectly aligned) at both the 3σ and 5σ level. Fortuitously, these extensions are also oriented such that we have the best spatial resolution in that direction. The $\alpha_{22-10\,\text{GHz}}$ spectral index map also shows two lobes of reduced spectral index (~ 0.5) in a similar direction to the extensions seen in the continuum. The combination of a low spectral index as well as perpendicular elongations may indicate the existence of a jet in VLA 1623 W. To confirm this, we would require higher-resolution and -sensitivity observations to pinpoint the origin of the outflow as well as any tenuous emission associated with it.

5. Conclusions

In this paper, we have investigated the protostellar system VLA 1623 using JWST, ALMA, and VLA. The high spatial resolution across each of the instruments (4–30 au) reveals unprecedented detail in one of the nearest young protostellar systems across nearly 4 orders of magnitude in wavelength. Below, we summarize our main findings.

1. Using JWST $4.44\,\mu\text{m}$ observations, we detect two outflow cavities in scattered light with origins that are cospatial with ALMA and VLA continuum observations of VLA 1623 Aa and B. The conical morphology and orientation of the emission suggests that these observations trace outflowing material from Aa and B. The proximity of the outflow cavity to Aa in addition to the flux increase and perpendicular morphology at 10 GHz implies this object is responsible for the large-scale outflow seen in VLA 1623.
2. VLA 1623 B appears to be a highly inclined disk at 217 and 93 GHz, with an optical depth surface for the former originating from $z/r \sim 0.3$, implying significant dust settling has yet to take place in the disk around this young Class 0 object. Based on the disk-to-star mass ratio of VLA 1623 B, it is possible that gravitational instabilities may be operating in the disk, which would naturally lead to an increased dust scale height.
3. Fitting the millimeter to centimeter SEDs for each object reveals that significant dust growth ($a_{\max} \gtrsim 1\,\text{mm}$) may have already taken place at these early stages of disk evolution. Furthermore, all objects appear to be optically thick at ALMA frequencies (217 GHz and 93 GHz) and dominated by ionized gas emission at low ($\lesssim 15\,\text{GHz}$) frequencies. For VLA 1623 B and W, the total dust mass is high ($\sim 100\text{s}\,M_\oplus$) and likely a lower limit due to the aforementioned high optical depths.
4. For frequencies below 44 GHz, we note nonnegligible contributions to the flux from the ionized gas components (e.g., $\gtrsim 5\%$–20%). This suggests frequencies between 44 and 93 GHz may offer the best trade-off between detecting optically thin dust emission while ensuring minimal contamination from ionized gas in YSOs, although this depends on the properties of the individual objects.

Our results represent some of the highest-resolution images currently available across these frequency regimes, particularly in the case of the A-configuration VLA observations. Despite this, much of our analysis is limited by the fact that we are unable to accurately resolve the emission morphology at frequencies below 22 GHz. Higher-resolution observations will only be available with next-generation interferometers operating at these frequencies, such as the Square Kilometre Array (SKA) and next-generation Very Large Array (ngVLA). At full capabilities, SKA-Mid will achieve angular resolutions approximately 6 times higher at 10 GHz than the observations we present here (55 mas; see R. Braun et al. 2019). The ngVLA will further increase this resolution by a factor of ~ 7 at the same frequencies (R. J. Selina et al. 2018). Such a leap in capability will be comparable to (or even better than) the highest-resolution infrared and (sub)millimeter observations currently available, opening the door to truly resolved studies of YSOs across several orders of magnitude in frequency for the first time.

Facilities: JWST (NIRCam), ALMA, VLA.

Software: CASA (The CASA Team et al. 2022), analysisUtils (T. R. Hunter et al. 2023), JWST Calibration Pipeline (H. Bushouse et al. 2023), Astropy (Astropy Collaboration et al. 2013, 2018, 2022), SciPy (P. Virtanen et al. 2020), PyBDSF (N. Mohan & D. Rafferty 2015), emcee (D. Foreman-Mackey et al. 2013), GoFish (R. Teague 2019).

Appendix A
Observational Details

Table A1 contains a summary of the observational setup of our ALMA and VLA observations. The table is divided into individual epochs and combined (fiducial) image parameters.

Table A1
Details of the ALMA and VLA Observations and Their Measured Properties for the Variability and Fiducial Image Products

Band	6	3	Q	K	X
Central wavelength	1.4 mm	3.2 mm	7.0 mm	1.4 cm	3.0 cm
Central frequency	217 GHz	93 GHz	44 GHz	22 GHz	10 GHz
Observing date (UT)	2021 Aug 7; 2021 Oct 3, 7	2021 Sep 7	2022 Apr 2, 7	2022 Apr 2, 7	2022 Apr 2, 7
Project code	2019.1.01074.S	2019.1.01074.S	22A-164	22A-164	22A-164
Configuration	C43-8	C43-9/10	A	A	A
Phase Center (J2000):					
R.A.	16:26:26.42	16:26:26.42	16:26:27.80	16:26:25.63	16:26:24.60
Decl.	−24.24.30.00	−24.24.30.00	−24.24.40.30	−24.24.29.4	−24.23.37.00
Primary beam size (FWHP)	27″	62″	1′.0	2′.0	4′.5
Maximum recoverable scale	0″.85	0″.86	1″.2	2″.4	5″.3
Total time on source (min)	86.8	84.5	60.7	28.7	5.5
Full bandwidth (GHz)	5.6	7.5	7.9	7.9	4
Gain calibrator	J1633-2557	J1633-2557	J1625-2527	J1625-2527	J1625-2527
Bandpass calibrator	J1337-1257	J1517-2422	J1256-0547	J1256-0547	J1256-0547
Flux calibrator	J1337-1257	J1517-2422	3C286	3C286	3C286
Variability Image properties:					
April 2					
Briggs Robust = 2.0					
Synthesized beam	⋯	⋯	0″.11 × 0″.1 [28°]	0″.26 × 0″.14 [26°]	0″.43 × 0″.19 [7°]
Cont. rms (mJy beam^{-1})[a]	⋯	⋯	0.03	0.01	0.03
April 7					
Briggs Robust = 2.0					
Synthesized beam	⋯	⋯	0″.11 × 0″.08 [8°]	0″.2 × 0″.18 [17°]	0″.42 × 0″.22 [6°]
Cont. rms (mJy beam^{-1})[a]	⋯	⋯	0.03	0.01	0.02
Fiducial Image properties:					
Briggs Robust = 0					
Synthesized beam	0″.06 × 0″.03 [60°]	0″.07 × 0″.05 [57°]	⋯	⋯	⋯
Cont. rms (mJy beam^{-1})[a]	0.02	0.01	⋯	⋯	⋯
Briggs Robust = 0.5					
Synthesized beam	⋯	⋯	0″.09 × 0″.06 [17°]	0″.18 × 0″.12 [19°]	0″.35 × 0″.16 [6°]
Cont. rms (mJy beam^{-1})[a]	⋯	⋯	0.02	0.009	0.01
Briggs Robust = 2.0					
Synthesized beam	⋯	⋯	⋯	0″.22 × 0″.16 [24°]	0″.42 × 0″.21 [7°]
Cont. rms (mJy beam^{-1})[a]	⋯	⋯	⋯	0.01	0.01
UVTaper = 0″.2 × 0″.08 [15°]					
Synthesized beam	⋯	⋯	0″.26 × 0″.14 [8°]	⋯	⋯
Cont. rms (mJy beam^{-1})[a]	⋯	⋯	0.03	⋯	⋯

Note.
[a] Measured at the centre of the primary beam.

Appendix B
Variability between VLA Epochs

Table B1 contains the fluxes extracted from both VLA epoch observations as well as the results of our variability analysis.

Table B1
Flux Comparison of VLA Observations at Each Epoch for a Robust Weighting of 2

Object	Frequency (GHz)	F_{min} (mJy)	F_{max} (mJy)	ΔF (mJy)	ΔF Error (mJy)	Variable?
VLA1623B	10	0.37	0.41	0.04	0.08	N
	22	0.98	1.09	0.11	0.15	N
	44	2.51	2.62	0.11	0.43	N
VLA1623Ab	10[a]	0.41	0.52	0.11	0.13	N
	22	0.41	0.50	0.09	0.08	N
	44	1.29	1.40	0.12	0.25	N
VLA1623Aa	10[a]	0.41	0.52	0.11	0.13	N
	22	0.46	0.46	0.00	0.07	N
	44	1.34	1.48	0.14	0.26	N
VLA1623W	10	0.25	0.25	0.04×10^{-1}	0.07	N
	22	0.35	0.37	0.02	0.07	N
	44[b]	…	…	…	…	…

Notes.
[a] VLA1623Aa and Ab are unresolved at the X band for a robust weighting 2 and thus share the same flux measurements.
[b] Image fidelity for each epoch makes accurate flux measurements unreliable to calculate.

Appendix C
SED Fluxes

Table C1 presents the full range of fluxes used in our SED fitting. These fluxes are taken from both this paper and the literature.

Table C1
Flux Measurements for Each Object Used in Figures 4 and 5

Object	Band	Frequency (GHz)	Robust	Total Flux (Jy)	Total Flux Error (Jy)
VLA 1623 Aa	C[a]	4.5	⋯	8.70×10^{-5}	3.03×10^{-5}
	C[a]	7.5	⋯	1.25×10^{-4}	2.57×10^{-5}
	X	10	0.5	2.33×10^{-4}	4.61×10^{-5}
	K	22	0.5	4.62×10^{-4}	5.00×10^{-5}
	Q	44	0.5	1.25×10^{-3}	1.56×10^{-4}
	B3	93	0.0	9.00×10^{-3}	4.50×10^{-4}
	B6	217	0.0	4.54×10^{-2}	4.54×10^{-3}
	B7[b]	350	⋯	1.93×10^{-1}	2.17×10^{-2}
VLA 1623 Ab	C[a]	4.5	⋯	8.70×10^{-5}	3.03×10^{-5}
	C[a]	7.5	⋯	1.25×10^{-4}	2.57×10^{-5}
	X	10	0.5	1.16×10^{-4}	3.27×10^{-5}
	K	22	0.5	4.40×10^{-4}	4.83×10^{-5}
	Q	44	0.5	1.24×10^{-3}	1.52×10^{-4}
	B3	93	0.0	8.76×10^{-3}	4.38×10^{-4}
	B6	217	0.0	3.97×10^{-2}	3.97×10^{-3}
	B7[b]	350	⋯	1.52×10^{-1}	1.63×10^{-2}
VLA 1623 B	C[a]	4.5	⋯	1.89×10^{-4}	3.52×10^{-5}
	C[a]	7.5	⋯	1.89×10^{-4}	3.52×10^{-5}
	X	10	0.5	3.55×10^{-4}	3.96×10^{-5}
	K	22	0.5	1.03×10^{-3}	1.09×10^{-4}
	Q	44	0.5	2.45×10^{-3}	3.09×10^{-4}
	B3	93	0.0	2.16×10^{-2}	1.08×10^{-3}
	B6	217	0.0	1.07×10^{-1}	1.07×10^{-2}
	B7[b]	350	⋯	3.21×10^{-1}	3.25×10^{-2}
VLA 1623 W	C[a]	4.5	⋯	2.18×10^{-4}	1.78×10^{-5}
	C[a]	7.5	⋯	1.98×10^{-4}	2.51×10^{-5}
	X	10	2.0	2.42×10^{-4}	3.84×10^{-5}
	K	22	2.0	3.68×10^{-4}	4.62×10^{-5}
	Q	44	2.0	4.90×10^{-4}	1.36×10^{-4}
	B3	93	0.0	8.20×10^{-3}	4.10×10^{-4}
	B6	217	0.0	5.18×10^{-2}	5.18×10^{-3}
	B7[b]	350	⋯	1.59×10^{-1}	1.67×10^{-2}

Notes.
[a] Taken from S. A. Dzib et al. (2013).
[b] Taken from R. J. Harris et al. (2018).

Appendix D
Astrometric Alignment

In Figure D1, we present the resulting image shifts from our image difference minimization discussed in Section 2.4. These shifts are used to overlay images for each frequency pair used in our spectral index map analysis (see Section 3.3). We quantify the difference between two images after each shift by considering the absolute value of the difference in pixel values, i.e., $|x_1 - x_2|$ where x_1 and x_2 are overlapping pixels from image 1 and image 2, respectively. Using this image difference metric, we normalize the value by the maximum difference from the shifts considered and refer to this as the normalized image difference, presented as the color scale in Figure D1.
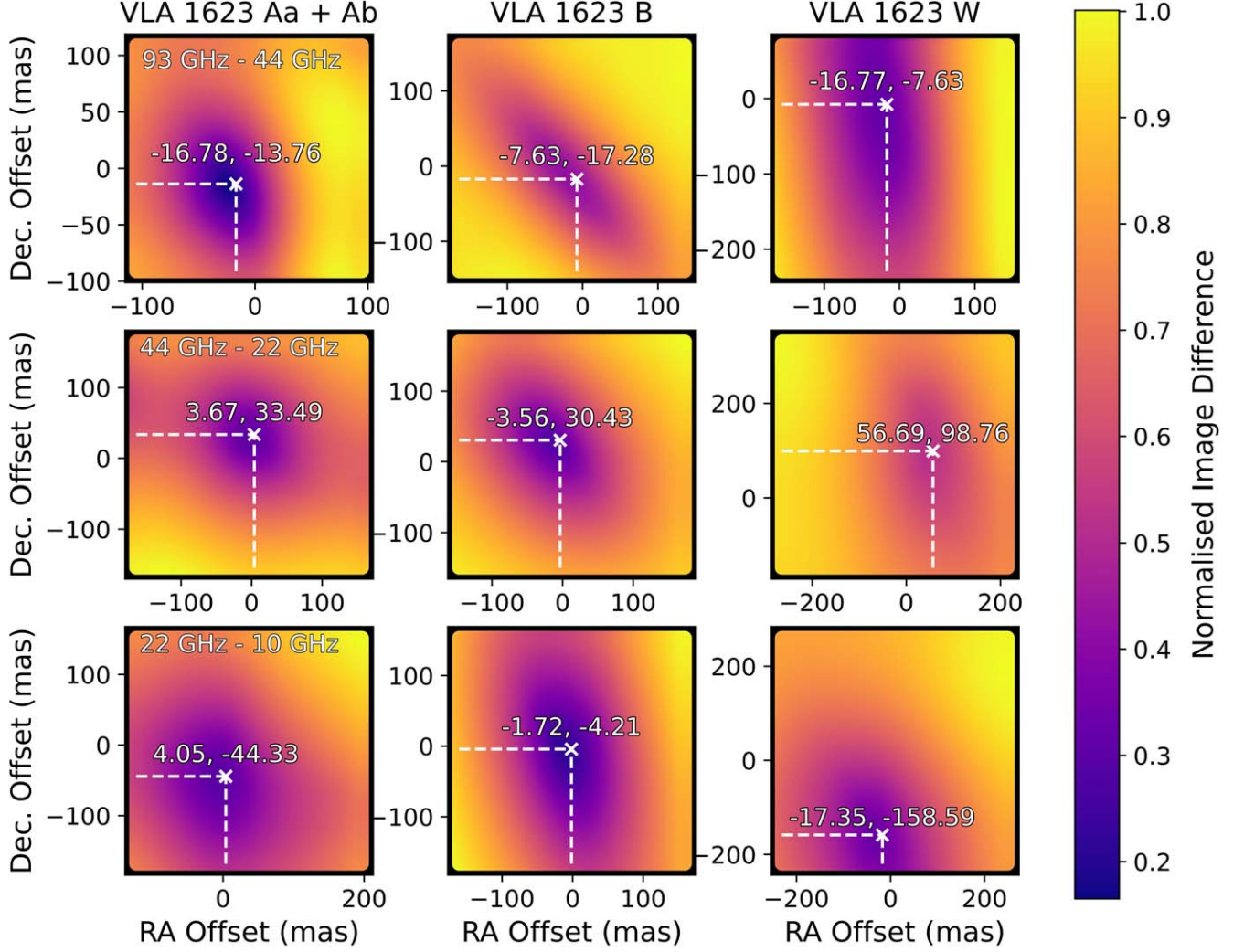
Figure D1 Following the methodology in Section 2.4 we present derived image shifts for each set of images used in Section 3.3. The color scale represents our image difference metric, normalized by the maximum image difference value in each object and frequency pair considered. We indicate the corresponding spectral index pair for each row in the top left of the first column. Each column is titled with the object(s) for which the minimization was performed. We indicate the optimal image shift as a white cross annotated with the value of the offsets.

Appendix E
SED Modeling with Multiple Dust Populations

E.1. Ionized Gas Emission

Following E. Keto ([2003](#)) and P. G. Mezger & A. P. Henderson ([1967](#)), we approximate $\tau_\nu^{\text{Ionized}}$ by:

$$\tau_\nu^{\text{Ionized}} = 8.235 \times 10^{-2} \left(\frac{T_e}{\text{K}}\right)^{-1.35} \left(\frac{\nu}{\text{GHz}}\right)^{-2.1}$$

$$\times \left(\frac{\text{EM}}{\text{pc cm}^{-6}}\right), \tag{E1}$$

where T_e is the electron temperature, and EM is the emission measure defined as $\text{EM} = \int n_e^2 \, d\ell$, and n_e is the electron number volume density. The flux density F_ν is given by

$$F_\nu = B_\nu(T_e)(1 - e^{-\tau_\nu^{\text{Ionized}}}) \Omega_{\text{Ionized}}, \tag{E2}$$

where Ω_{Ionized} is the observed solid angle, and $B_\nu(T) = (2h\nu^3/c^2)(e^{h\nu/k_B T} - 1)^{-1}$ is the Planck function at temperature T_e, and h and k_B are the Planck and Boltzmann constants.

The ionized gas emission is optically thick at low frequencies, with spectral index α as high as 2.0; it is optically thin at high frequencies where α can be as low as -0.1. Given T_e, the turnover frequency that separates the optically thick and thin regime is determined by EM.

E.2. Multiple Dust Populations

In order to more accurately describe the SEDs of each source in Section [3.2.2](#), we must use a minimum of 10 free parameters, i.e., T_{dust}, Σ_{dust}, a_{max}, and Ω_{dust} for two dust components, as well as EM and Ω_{Ionized} for the ionized gas component. Moreover, we found that the SEDs of our target sources are not necessarily consistent with uniform T_{dust}, Σ_{dust}, and a_{max}.

To explain the strong emission at centimeter wavelengths, we needed to assume the geometry that dust components with higher T_{dust} are obscured by dust components with lower T_{dust} in the line of sight, which is an assumption that is often needed in the modeling of the (sub)millimeter SEDs of deeply embedded Class 0/I objects (see, J. I.-H. Li et al. [2017](#)). In addition, we found that the higher T_{dust} components in a source may have higher a_{max} and/or higher Σ_{dust} than the lower T_{dust} components, although the values of Σ_{dust} and a_{max} are degenerate in our models. As a consequence, we require more free parameters to describe the SEDs of each object. However, since our SEDs include at most eight independent measurements for each source, the parameters for our SED models are
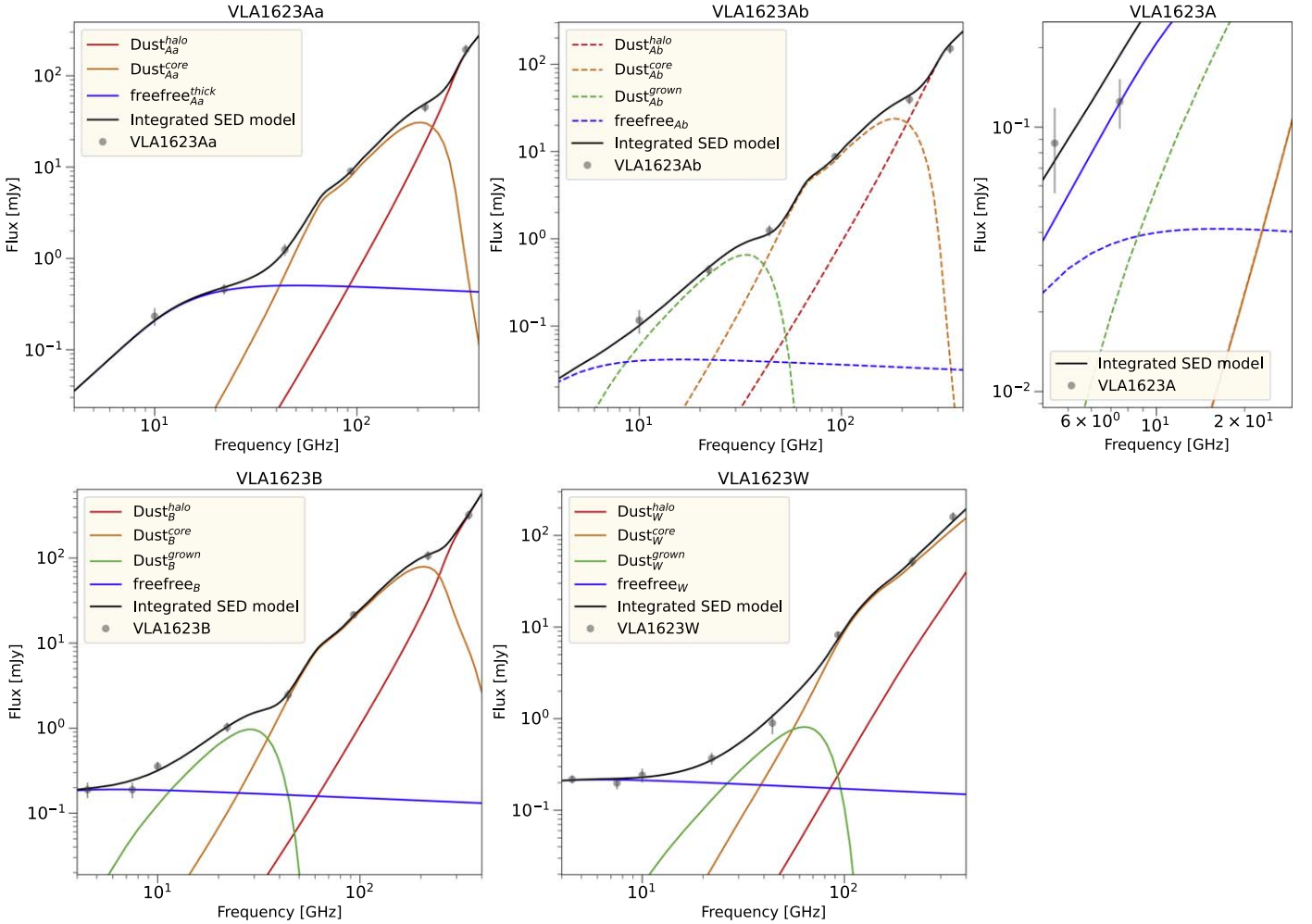
Figure E1 Top panel: SED models for the VLA 1623 Aa and Ab resolved, integrated fluxes alongside the combined model, A, for the unresolved *C*-band data (S. A. Dzib et al. [2013](#)). Symbols show the observational data, and colored lines show the SEDs of individual emission components in our model (Table [E1](#)). For clarity, we show the Aa emission components as solid lines and Ab components as dashed lines in the combined model. Integrated flux densities are shown in black lines. Bottom panel: same as the top panel but for resolved observations of VLA 1623 B and W, respectively.

Table E1
Model Parameters That Reproduce the Observed SEDs

Component	T (K)	Ω[a] (10^{-12} sr)	Σ_{dust} (g cm^{-2})	a_{max} (mm)	EM (cm^{-6} pc)	Obscured by	M_{dust} $M_{\oplus}$
	(1)	(2)	(3)	(4)	(5)	(6)	(7)
VLA 1623 Aa							
Halo	170	0.63	0.25	0.2	⋯		4.4
Core	200	0.32	6.0	0.8	⋯	Halo	52
Ionized gas	8000	9×10^{-3}	⋯	⋯	8×10^{8}		⋯
							Total: 56.4
VLA 1623 Ab							
Halo	170	0.5	0.4	0.2	⋯		5.4
Core	240	0.27	6.0	0.8	⋯	Halo	45
Grown	340	0.2	20	15	⋯	Halo+Core	110
Ionized gas	8000	7×10^{-3}	⋯	⋯	7.5×10^{7}		⋯
							Total: 160
VLA 1623 B							
Halo	120	2.2	0.15	0.22	⋯		9.1
Core	153	1.18	6.0	1.0	⋯	Halo	194
Grown	180	0.8	20	15	⋯	Halo+Core	440
Ionized gas	8000	0.22	⋯	⋯	1.0×10^{7}		⋯
							Total: 643
VLA 1623 W							
Halo	20	3.5	0.2	0.05	⋯		19
Core	20	4.0[a]	3.5	0.4	⋯	Halo	384
Grown	120	0.2	20	15	⋯	Halo+Core	110
Ionized gas	8000	0.25	⋯	⋯	1.0×10^{7}		⋯
							Total: 513

Note. Similar to Table 2 but including multiple, mutually obscuring dust components for each source. In column (6) we include the components that are obscuring the emission of this component.

[a] 1 sr $\sim 4.25 \times 10^{10}$ square arcsecond.

inevitably degenerate. Therefore, we do not run systematic fittings (e.g., χ^2 fittings or MCMC), and thus these models should be understood in a qualitative sense, as probable rather than unique solutions. Nevertheless, our SED models still provide some general understanding of the target sources and some physical implications.

We present our SED models for the four target sources in Figure E1 with the model parameters, summarized in Table E1. The names of the SED components we use in the model are for our convenience to reference them in text and do not have strict physical meanings. Below we discuss the specific fitting methodology used for each source.

VLA 1623 A. The binary components, Aa and Ab, were spatially resolved between 10 and 217 GHz (see Figure 3). However, they were not resolved in the previous VLA C band (4.5 GHz and 7.5 GHz) observations (S. A. Dzib et al. 2013). The intra-band spectral index ($\alpha_{7.5-4.5\ GHz}$) is $\sim$0.7, which is consistent with ionized gas emission (see Appendix E1). In at least one of the two binary components, ionized gas emission partly contributes to the integrated SEDs. The fractional contribution of ionized gas emission may be higher in Aa, as Aa is considerably brighter than Ab in the resolved 10 GHz continuum image.

At frequencies >20 GHz, the spectral shapes and flux densities of Aa and Ab are similar (Figure E1). Their 350–217 GHz spectral indices are $\sim$3, while the spectral indices between 22 GHz and 217 GHz are close to 2. In both binary components, the 350 GHz flux densities are likely contributed by dust thermal emission from the relatively

spatially extended, marginally optically thin halos (hereafter the "halo" components), which may represent the outer disks or inner envelopes. At $\sim$20–200 GHz, the flux densities may be partly or largely contributed by the thermal emission of the relatively spatially compact, optically thick disk cores (hereafter, the "core" components).

The dust temperatures and solid angles of the halo and core components in Aa and Ab were (loosely) constrained thanks to the high angular resolutions of the 350 and 217 GHz observations. We approximated the solid angles of the halos components according to the deconvolved size scales at 350 GHz (see Table 2 in R. J. Harris et al. 2018), and adjusted the dust temperatures to make the flux densities consistent with the observations at 350 and 217 GHz. The "core" components need to be obscured by the "halo" components in the line of sight to suppress the contribution of the "core" components at >217 GHz. Otherwise, in the integrated SEDs, the strong contribution from the "core" components will yield 350–217 GHz spectral index values that are too low to be consistent with observations (Figure E1). Therefore, we make the T_{dust}/Ω_{dust} slightly larger/smaller than those of the "halo" components, while we note that there is a degeneracy between these two parameters.

The Σ_{dust} of the "halo" components were constrained by the 350–217 GHz spectral indices. The a_{max} in the "halo" components were not well constrained. We found that $a_{max} = 200\ \mu$m may be a good solution, which provides modest extinction opacity at the required emission optical depths.
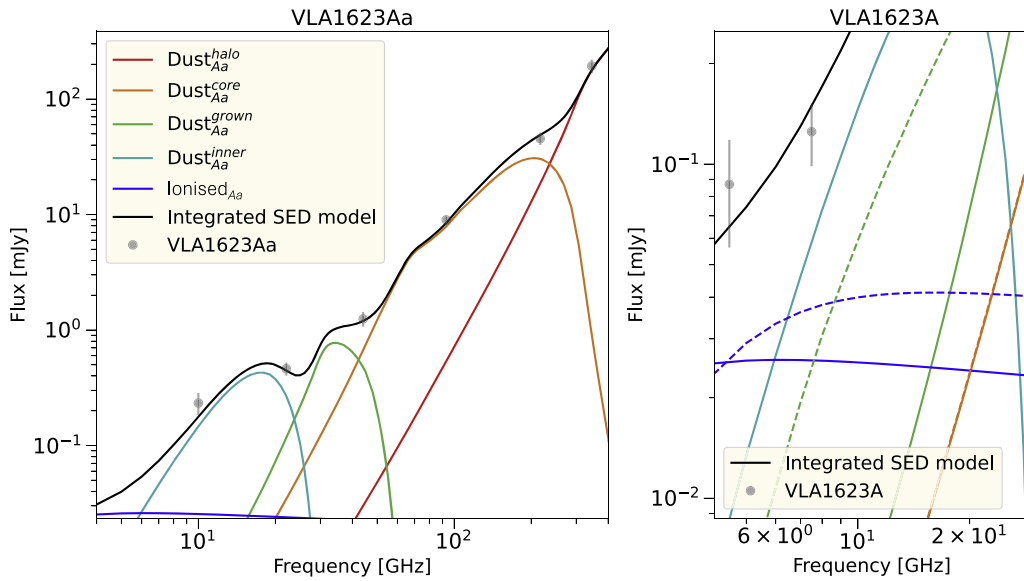
Figure E2 Embedded "hot dust" SED model for the VLA 1623 Aa resolved, integrated fluxes alongside the combined model for the unresolved *C*-band data (S. A. Dzib et al. 2013). Symbols show the observational data, and colored lines show the SEDs of individual emission components in our model (Table E2). We show the SED model components for Ab as dashed lines in the combined model plot.

The 217–93 GHz spectral indices provided the lower limits for the Σ_{dust} of the "core" components. The a_{max} of the "core" components were once again barely constrained. We found that choosing $a_{max} \sim 0.8$ mm helps maintain the constant ~ 2 spectral indices between 44 GHz and 217 GHz, and provides sufficient extinction opacity at lower frequencies (explained below). Fixing a_{max} to 0.8 mm, we adjusted the Σ_{dust} of the "core" components to make them optically thick at $\gtrsim 50$ GHz (Figure E1). In this case, the dust masses in the "core" components are $\sim 50 \, M_{\oplus}$, which may be regarded as lower limits (Table E1). Operationally, we can continue increasing the Σ_{dust} of the "core" components until their flux densities meet those observed at 10 and 22 GHz. In that case, the dust masses in the "core" components will be further enhanced by 1–2 orders or magnitudes, which is not necessarily realistic.

VLA 1623 Aa. The simplest model to interpret the bright 10–22 GHz emission in VLA 1623 Aa (and part, if not all, of the 4.5 GHz and 7.5 GHz emission in the binary system) is with an ionized gas emission component that has a turnover frequency around 10–22 GHz (see the top-left panel of Figure E1; Table E1; see Appendix E.1). However, the parameters are uncertain, as the *C*-band measurements were taken well before our VLA observations, and we are not yet certain about the radio variability of this source (e.g., S. A. Dzib et al. 2013; H. B. Liu et al. 2014; A. Coutens et al. 2019).

In addition, we note that the lower limit of the 10–7.5 GHz spectral index in Aa is ~ 2.0. Although this spectral index is consistent with optically thick ionized gas emission, there are currently no observations that can confirm whether or not an optically thick ionized gas emission source can exist in a low-mass YSO. The existing analytic models of ionized wind and jets that dominate the ionized gas emission in low-mass YSOs present surface density gradients. Therefore, the spatially unresolved radio observations (e.g., 7.5–10 GHz) will always simultaneously detect the optically thick wind/jet core with a spectral index ~ 2.0, in combination with the optically thin component that has a lower spectral index, i.e., <2. In this case,

the spectral indices of a relatively optically thick ionized wind/jet are expected to be ~ 0.6, which is considerably lower than the lower limit constrained at 10–7.5 GHz (A. E. Wright & M. J. Barlow 1975; S. P. Reynolds 1986; G. Anglada et al. 1998).

Due to the rationale discussed above, it may not be favorable to fully attribute the 10–22 GHz emission in source Aa to ionized gas emission. We discuss an alternative interpretation in Appendix E.3 where part of the 10–22 GHz emission may be contributed by large embedded hot dust.

VLA 1623 Ab. The 22–10 GHz spectral index of source Ab is considerably higher than that in source Aa. Therefore, the 10 and 22 GHz flux densities cannot be dominated by ionized gas emission. We found that we can sufficiently reproduce the flux densities at the VLA bands by including a $T_{dust} = 340$ K component, namely the "grown" component (Table E1). The a_{max} is not constrained by our current observations. We tentatively chose $a_{max} = 15$ mm to yield a high emissivity at 10 and 22 GHz. The dust mass of this component is $\sim 111 \, M_{\oplus}$, which should be regarded as a lower limit.

VLA 1623 B and W. Following the same methodology outlined above for VLA 1623 A, we find that the resulting SED models of VLA 1623 B and W are qualitatively similar to the model for VLA 1623 Ab. Both VLA 1623 B and W require a "grown" component to reconcile the fluxes at the VLA bands. However, in contrast to Aa, both B and W also require the inclusion of an optically thin ionized gas emission source to reproduce the observed spectral indices at low frequencies. This is due to their intra-band spectral indices ($\alpha_{7.5–4.5 \, GHz}$) of <-0.1 (see, e.g., S. A. Dzib et al. 2013), which are inconsistent with dust emission alone.

E.3. Embedding Hot Dust Emission Components

Previous SED modeling analyses have shown that embedding high-temperature dust emission components that have relatively small Ω_{dust} can reproduce the bright emission and low spectral indices seen at low frequencies (J. I.-H. Li et al.

Table E2
Model Parameters

Component	T (K) (1)	Ω^a (10^{-12} sr) (2)	Σ_{dust} (g cm^{-2}) (3)	a_{max} (mm) (4)	EM (cm^{-6} pc) (5)	Obscured by (6)	M_{dust} $M_\oplus$ (7)
VLA 1623 Aa							
Halo	170	0.63	0.25	0.2	…		4.4
Core	200	0.32	6.0	0.8	…	Halo	53
Grown	400	0.27	8.0	1.8	…	Halo+Core	60
Inner	1200	0.2	10	25	…	Halo+Core+Grown	55
Ionized gas	8000	$3 \cdot 10^{-2}$	…	…	$1 \cdot 10^7$		…
							Overall: 172

Note. Column: (1) Dust temperature for dust emission components and electron temperature for the ionized gas emission component. Column: (2) Solid angle of the emission components. Column: (3) Dust column density. Column: (4) Maximum (dust) grain size. Column: (5) Emission measure for the ionized gas emission component. Column: (6) The components that are obscuring the emission of this component. Column: (7) Dust mass in units of Earth mass ($M_\oplus$).
a 1 sr $\sim 4.25 \times 10^{10}$ square arcsecond.

2017; H. B. Liu et al. 2019). By assuming millimeter- or centimeter-sized a_{max}, one can achieve bright emission at VLA bands.

In Figure E2, we present a model that can reproduce the observed flux densities by progressively embedding higher temperature and larger a_{max} dust emission components on smaller scales (namely the "grown," and "inner" components; see Table E2). Including the "grown" component and making it obscured by the "core" component allows the model to maintain the high flux density and flat spectral profile at 44–22 GHz; including the "inner" component and making it obscured by the "grown" component allows maintaining the high flux density and flat spectral profile at 22–10 GHz. We note that the wiggles in the SED model are artificial and are a result of the discrete emission components we use to approximate the SED. These wiggles can be eliminated by adopting an analytic model that has continuous density and temperature profiles, which is beyond the scope of the present paper.

In the present model, the a_{max} of the "core," "grown," and "inner" components were chosen such that the dust emission components have high absorption opacities and modest extinction opacities at 22 GHz and 10 GHz. In this case, the model provides the relatively conservative dust mass estimates for the embedded dust emission components, which may be regarded as lower limits (Table E1).

The Ω_{dust}, a_{max}, T_{dust}, and Σ_{dust} are degenerate due to the limited independent observational constraints. Nevertheless, we note that assuming smaller dust sizes (e.g., $a_{max} \lesssim 100\ \mu m$) will yield considerably higher dust masses, which are not necessarily realistic. We also note that the upper limit of T_{dust} is the $\sim$1500 K sublimation temperature. We summarize the probable model parameters in Table E2.

ORCID iDs

Isaac C. Radley ⓘ https://orcid.org/0009-0007-2837-8207
Gemma Busquet ⓘ https://orcid.org/0000-0002-2189-6278
John D. Ilee ⓘ https://orcid.org/0000-0003-1008-1142
Hauyu Baobab Liu ⓘ https://orcid.org/0000-0003-2300-2626
Jaime E. Pineda ⓘ https://orcid.org/0000-0002-3972-1978
Klaus M. Pontoppidan ⓘ https://orcid.org/0000-0001-7552-1562
Enrique Macías ⓘ https://orcid.org/0000-0003-1283-6262
María José Maureira ⓘ https://orcid.org/0000-0002-7026-8163
Eleonora Bianchi ⓘ https://orcid.org/0000-0001-9249-7082
Tyler L. Bourke ⓘ https://orcid.org/0000-0001-7491-0048
Claudio Codella ⓘ https://orcid.org/0000-0003-1514-3074
Jan Forbrich ⓘ https://orcid.org/0000-0001-8694-4966
Josep M. Girart ⓘ https://orcid.org/0000-0002-3829-5591
Melvin G. Hoare ⓘ https://orcid.org/0000-0003-2684-399X
Ricardo Hernández Garnica ⓘ https://orcid.org/0000-0002-4762-2240
Izaskun Jiménez-Serra ⓘ https://orcid.org/0000-0003-4493-8714
Laurent Loinard ⓘ https://orcid.org/0000-0002-5635-3345
Jazmín Ordóñez-Toro ⓘ https://orcid.org/0000-0001-7776-498X
Linda Podio ⓘ https://orcid.org/0000-0003-2733-5372

References

Andre, P., Martin-Pintado, J., Despois, D., & Montmerle, T. 1990, A&A, 236, 180
Andre, P., Ward-Thompson, D., & Barsony, M. 1993, ApJ, 406, 122
Andrews, S. M., Huang, J., Pérez, L. M., et al. 2018, ApJL, 869, L41
Anglada, G., Rodrìguez, L. F., & Carrasco-González, C. 2018, A&ARv, 26, 3
Anglada, G., Villuendas, E., Estalella, R., et al. 1998, AJ, 116, 2953
Ansdell, M., Williams, J. P., van der Marel, N., et al. 2016, ApJ, 828, 46
Artymowicz, P., & Lubow, S. H. 1994, ApJ, 421, 651
Astropy Collaboration, Price-Whelan, A. M., Lim, P. L., et al. 2022, ApJ, 935, 167
Astropy Collaboration, Price-Whelan, A. M., Sipőcz, B. M., et al. 2018, AJ, 156, 123
Astropy Collaboration, Robitaille, T. P., Tollerud, E. J., et al. 2013, A&A, 558, A33
Avenhaus, H., Quanz, S. P., Garufi, A., et al. 2018, ApJ, 863, 44
Bae, J., Hartmann, L., & Zhu, Z. 2015, ApJ, 805, 15
Birnstiel, T., Dullemond, C. P., Zhu, Z., et al. 2018, ApJL, 869, L45
Boley, A. C., & Durisen, R. H. 2006, ApJ, 641, 534
Bontemps, S., & Andre, P. 1997, in IAU Symp.182, Herbig-Haro Flows and the Birth of Stars, ed. B. Reipurth & C. Bertout (Cambridge: Cambridge Univ. Press), 63
Braun, R., Bonaldi, A., Bourke, T., Keane, E., & Wagg, J. 2019, arXiv:1912.12699
Bushouse, H., Eisenhamer, J., Dencheva, N., et al. 2023, JWST Calibration Pipeline, v1.12.5, Zenodo, doi:10.5281/zenodo.10022973
Caratti o Garatti, A., Giannini, T., Nisini, B., & Lorenzetti, D. 2006, A&A, 449, 1077
Carrasco-González, C., Sierra, A., Flock, M., et al. 2019, ApJ, 883, 71
Chiang, E. I., & Goldreich, P. 1997, ApJ, 490, 368
Chung, C.-Y., Andrews, S. M., Gurwell, M. A., et al. 2024, ApJS, 273, 29
Cieza, L. A., Ruìz-Rodrìguez, D., Hales, A., et al. 2019, MNRAS, 482, 698
Claude, S., Jiang, F., Niranjanan, P., et al. 2008, Proc. SPIE, 7020, 70201B
Codella, C., Ceccarelli, C., Chandler, C., et al. 2021, FrASS, 8, 227
Codella, C., Podio, L., De Simone, M., et al. 2024, MNRAS, 528, 7383
Condon, J. J., & Ransom, S. M. 2016, Essential Radio Astronomy (Princeton, NJ: Princeton Univ. Press)

Coutens, A., Liu, H. B., Jiménez-Serra, I., et al. 2019, A&A, 631, A58
Davis, C. J., & Eisloeffel, J. 1995, A&A, 300, 851
Delussu, L., Birnstiel, T., Miotello, A., et al. 2024, A&A, 688, A81
Dent, W. R. F., Matthews, H. E., & Walther, D. M. 1995, MNRAS, 277, 193
Díaz-Márquez, E., Grau, R., Busquet, G., et al. 2024, A&A, 682, A180
Draine, B. T. 2003, ARA&A, 41, 241
Draine, B. T. 2006, ApJ, 636, 1114
Duchêne, G., Ménard, F., Stapelfeldt, K. R., et al. 2024, AJ, 167, 77
Dulk, G. A. 1985, ARA&A, 23, 169
Dzib, S. A., Loinard, L., Mioduszewski, A. J., et al. 2013, ApJ, 775, 63
Ediss, G. A., Carter, M., Cheng, J., et al. 2004, in 15th Int. Symp. on Space Terahertz Technology, ed. G. Narayanan (Northampton, MA) 181
Fazio, G. G., Hora, J. L., Allen, L. E., et al. 2004, ApJS, 154, 10
Feigelson, E. D., & Montmerle, T. 1985, in Astrophysics and Space Science Library, Vol. 116, Radio Stars, ed. R. M. Hjellming & D. M. Gibson (Dordrecht: Reidel), 335
Foreman-Mackey, D., Hogg, D. W., Lang, D., & Goodman, J. 2013, PASP, 125, 306
Friesen, R. K., Pineda, J. E., co-PIs, et al. 2017, ApJ, 843, 63
Ginski, C., Garufi, A., Benisty, M., et al. 2024, A&A, 685, A52
Guerra-Alvarado, O. M., van der Marel, N., Di Francesco, J., et al. 2024, A&A, 681, A82
Han, I., Kwon, W., Aso, Y., Bae, J., & Sheehan, P. 2023, ApJ, 956, 9
Hara, C., Kawabe, R., Nakamura, F., et al. 2021, ApJ, 912, 34
Harris, R. J., Cox, E. G., Looney, L. W., et al. 2018, ApJ, 861, 91
Henning, T., & Stognienko, R. 1996, A&A, 311, 291
Högbom, J. A. 1974, A&AS, 15, 417
Hsieh, C.-H., Arce, H. G., Maureira, M. J., et al. 2024, ApJ, 973, 138
Hsieh, C.-H., Lai, S.-P., Cheong, P.-I., et al. 2020, ApJ, 894, 23
Huang, J., Andrews, S. M., Pérez, L. M., et al. 2018, ApJL, 869, L43
Hunter, T. R., Petry, D., Barkats, D., Corder, S., & Indebetouw, R. 2023, AnalysisUtils, v2.6, Zenodo, doi:10.5281/zenodo.7502160
Johansen, A., Blum, J., Tanaka, H., et al. 2014, in Protostars and Planets VI, ed. H. Beuther et al. (Tuscon, AZ: Univ. Arizona Press), 547
Kataoka, A., Muto, T., Momose, M., et al. 2015, ApJ, 809, 78
Kawabe, R., Hara, C., Nakamura, F., et al. 2018, ApJ, 866, 141
Keto, E. 2003, ApJ, 599, 1196
Kratter, K., & Lodato, G. 2016, ARA&A, 54, 271
Kuznetsova, A., Bae, J., Hartmann, L., & Mac Low, M.-M. 2022, ApJ, 928, 92
Law, C. J., Teague, R., Öberg, K. I., et al. 2023, ApJ, 948, 60
Li, J. I.-H., Liu, H. B., Hasegawa, Y., & Hirano, N. 2017, ApJ, 840, 72
Lin, Z.-Y. D., Li, Z.-Y., Tobin, J. J., et al. 2023, ApJ, 951, 9
Liu, H. B. 2019, ApJL, 877, L22
Liu, H. B. 2021, ApJ, 914, 25
Liu, H. B., Galván-Madrid, R., Forbrich, J., et al. 2014, ApJ, 780, 155
Liu, H. B., Mérand, A., Green, J. D., et al. 2019, ApJ, 884, 97
Liu, H. B., Tsai, A.-L., Chen, W. P., et al. 2021, ApJ, 923, 270
Long, F., Herczeg, G. J., Harsono, D., et al. 2019, ApJ, 882, 49
Looney, L. W., Mundy, L. G., & Welch, W. J. 2000, ApJ, 529, 477
Macías, E., Anglada, G., Osorio, M., et al. 2016, ApJ, 829, 1
Manara, C. F., Tazzari, M., Long, F., et al. 2019, A&A, 628, A95
Mayer, L., Quinn, T., Wadsley, J., & Stadel, J. 2004, ApJ, 609, 1045
Mercimek, S., Podio, L., Codella, C., et al. 2023, MNRAS, 522, 2384
Mezger, P. G., & Henderson, A. P. 1967, ApJ, 147, 471
Michel, A., Sadavoy, S. I., Sheehan, P. D., Looney, L. W., & Cox, E. G. 2022, ApJ, 937, 104

Mohan, N., & Rafferty, D., 2015 PyBDSF: Python Blob Detection and Source Finder, Astrophysics Source Code Library, ascl:1502.007
Murillo, N. M., Harsono, D., McClure, M., Lai, S. P., & Hogerheijde, M. R. 2018a, A&A, 615, L14
Murillo, N. M., & Lai, S.-P. 2013, ApJL, 764, L15
Murillo, N. M., Lai, S.-P., Bruderer, S., Harsono, D., & van Dishoeck, E. F. 2013, A&A, 560, A103
Murillo, N. M., van Dishoeck, E. F., van der Wiel, M. H. D., et al. 2018b, A&A, 617, A120
Narayanan, S., Williams, J. P., Tobin, J. J., et al. 2023, ApJ, 958, 20
Nisini, B., Santangelo, G., Giannini, T., et al. 2015, ApJ, 801, 121
Ohashi, N., Tobin, J. J., Jørgensen, J. K., et al. 2023, ApJ, 951, 8
Ohashi, S., Codella, C., Sakai, N., et al. 2022, ApJ, 927, 54
Okuzumi, S., Momose, M., Sirono, S.-i., Kobayashi, H., & Tanaka, H. 2016, ApJ, 821, 82
Ortiz-León, G. N., Loinard, L., Dzib, S. A., et al. 2018, ApJL, 869, L33
Pascucci, I., Cabrit, S., Edwards, S., et al. 2023, in ASP Conf. Ser. 534, Protostars and Planets VII, ed. S. Inutsuka et al. (San Francisco, CA: ASP), 567
Pascucci, I., Gorti, U., & Hollenbach, D. 2012, ApJL, 751, L42
Pech, G., Loinard, L., Chandler, C. J., et al. 2010, ApJ, 712, 1403
Pinte, C., Dent, W. R. F., Ménard, F., et al. 2016, ApJ, 816, 25
Pontoppidan, K. M., Barrientes, J., Blome, C., et al. 2022, ApJL, 936, L14
Ray, T. P., & Ferreira, J. 2021, NewAR, 93, 101615
Reynolds, S. P. 1986, ApJ, 304, 713
Ridge, N. A., Di Francesco, J., Kirk, H., et al. 2006, AJ, 131, 2921
Rieke, M. J., Kelly, D. M., Misselt, K., et al. 2023, PASP, 135, 028001
Sadavoy, S. I., Sheehan, P., Tobin, J. J., et al. 2024, A&A, 687, A308
Sadavoy, S. I., Stephens, I. W., Myers, P. C., et al. 2019, ApJS, 245, 2
Santangelo, G., Murillo, N. M., Nisini, B., et al. 2015, A&A, 581, A91
Segura-Cox, D. M., Schmiedeke, A., Pineda, J. E., et al. 2020, Natur, 586, 228
Selina, R. J., Murphy, E. J., McKinnon, M., et al. 2018, in ASP Conf. Ser. 517, Science with a Next Generation Very Large Array, ed. E. Murphy (San Francisco, CA: ASP), 15
Sierra, A., & Lizano, S. 2020, ApJ, 892, 136
Takakuwa, S., Saigo, K., Kido, M., et al. 2024, ApJ, 964, 24
Tazaki, R., Tanaka, H., Kataoka, A., Okuzumi, S., & Muto, T. 2019, ApJ, 885, 52
Teague, R. 2019, JOSS, 4, 1632
The CASA Team, Bean, B., Bhatnagar, S., et al. 2022, PASP, 134, 114501
Tobin, J. J., van't Hoff, M. L. R., Leemker, M., et al. 2023, Natur, 615, 227
Tsukamoto, Y., Okuzumi, S., & Kataoka, A. 2017, ApJ, 838, 151
Ubach, C., Maddison, S. T., Wright, C. M., et al. 2017, MNRAS, 466, 4083
Villenave, M., Benisty, M., Dent, W. R. F., et al. 2019, A&A, 624, A7
Villenave, M., Podio, L., Duchêne, G., et al. 2023, ApJ, 946, 70
Virtanen, P., Gommers, R., Oliphant, T. E., et al. 2020, NatMe, 17, 261
Vorobyov, E. I., & Basu, S. 2006, ApJ, 650, 956
Warren, S. G. 1984, ApOpt, 23, 1206
Weidenschilling, S. J. 1977, Ap&SS, 51, 153
Wilking, B. A., Lada, C. J., & Young, E. T. 1989, ApJ, 340, 823
Wright, A. E., & Barlow, M. J. 1975, MNRAS, 170, 41
Xu, W. 2022, ApJ, 934, 156
Xu, W., Ohashi, S., Aso, Y., & Liu, H. B. 2023, ApJ, 954, 190
Zamponi, J., Maureira, M. J., Zhao, B., et al. 2021, MNRAS, 508, 2583
Zhang, M., & Wang, H. 2009, AJ, 138, 1830
Zhu, Z., Zhang, S., Jiang, Y.-F., et al. 2019, ApJL, 877, L18